5-10-2022

Optimization of paper-based substrates for surface enhanced raman spectroscopic biosensor development

Kaylee M. Cappuccio
Binghamton University--SUNY, kcappuc1@binghamton.edu

OPTIMIZATION OF PAPER-BASED SUBSTRATES FOR SURFACE ENHANCED RAMAN SPECTROSCOPIC BIOSENSOR DEVELOPMENT

BY

KAYLEE M. CAPPUCCIO

BS, STATE UNIVERSITY OF NEW YORK AT BINGHAMTON, 2022

HONORS THESIS

Submitted in partial fulfillment of the requirements for
Distinguished Independent Work in Chemistry
in the Harpur College of
Binghamton University
State University of New York
2022

Accepted in partial fulfillment of the requirements for
Distinguished Independent Work in Chemistry
in the Harpur College of
Binghamton University
State University of New York
2022

May 10th, 2022

Dr. Chuan-Jian Zhong, Faculty Advisor
Department of Chemistry, Binghamton University

Dr. Rebecca Kissling, Member
Department of Chemistry, Binghamton University

Dr. Christof Grewer, Member
Department of Chemistry, Binghamton University

Dr. Clarice Kelleher, Member
Department of Chemistry, Binghamton University

Abstract

Advancements in the field of analytical chemistry have greatly expanded the development of biosensors for the detection of a wide array of diseases. This study aims to optimize an affordable paper-based nanocomposite biosensor that utilizes surface-enhanced Raman spectroscopy (SERS). Specifically, it investigates the preparation parameters for a paper-based SERS substrate, including nanoparticle administration and drying procedures. A particular focus of this work is to assess how the wax-defined paper channels can effectively enhance SERS intensity. The results revealed that while the wax-printed wells can define the nanoparticle administration for SERS detection, wax backing may reduce the sensitivity of SERS by preventing two-directional solution drying, promoting a non-uniform distribution of nanoparticles on paper substrates. The limit of detection in terms of the number of nanoparticles within the paper-based SERS platform was determined, showing a limit of detection of 0.02% of a theoretical monolayer of gold nanoparticles. These findings, along with preliminary on-going work, suggest that this platform can be expanded with the use of click chemistry for the development of highly sensitive paper-based microfluidic SERS biosensors for the detection of biomarkers in various diseases, such as Severe Acute Respiratory Syndrome Coronavirus 2 (SARS-CoV-2).

Table of Contents

List of Figures

List of Abbreviations

SERS	Surface-enhanced Raman Spectroscopy
SARS-CoV-2	Severe Acute Respiratory Syndrome Coronavirus 2
SPR	Surface plasmon resonance
MBA	4-mercaptobenzoic acid
UV-vis	Ultraviolet-visible spectroscopy
TEM	Transmission electron microscopy
NP	Nanoparticle
EDC	N-(3-Dimethylaminopropyl)-N'-ethylcarbodiimide hydrochloride
S-NHS	N-Hydroxysulfosuccinimide
N-Protein	Nucleocapsid Protein
LUMO	Lowest unoccupied molecular orbital
HOMO	Highest occupied molecular orbital

1. INTRODUCTION

This work focuses on investigating the parameters for optimizing a wax-printed paper-based surface-enhanced Raman spectroscopic (SERS) substrate, including nanoparticle administration and mode of drying. It additionally assesses the limit of detection in terms of the number of nanoparticles (NPs) present within wax-defined wells for the development of a paper-based SERS biosensor platform, which are outlined in Figure 1.

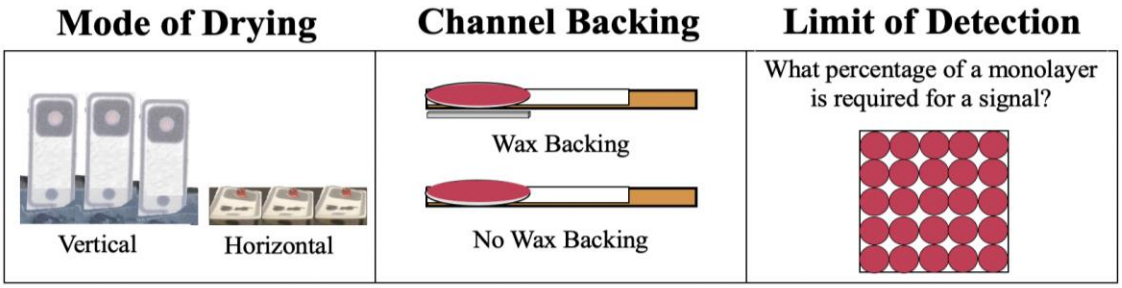

Figure 1. Overview of the paper-based SERS platform parameters investigated in this work.

This section first gives overviews of biosensors, SERS detection enhancement by plasmonic nanoparticles, and the paper-based SERS substrates. These overviews are followed by an outline of the objectives and approaches employed in this work.

1.1 Overview of Biosensors

In recent years, the field of analytical chemistry has greatly expanded the development and optimization of biosensors.[1] At the most basic level, biosensors contain analytes, or substances to be detected, bioreceptors, transducers, electronics, and displays.[2] A bioreceptor is a biomolecule (i.e., antibody or enzyme) that can detect the presence of an analyte, while a transducer is responsible for turning the bio-recognition between an analyte and a biomolecule into a signal.[2] Electronics can then transform the

signal into an output for the display, enabling the detection and quantification of a biological analyte of interest.[2] Figure 2 summarizes the elements of a biosensor.

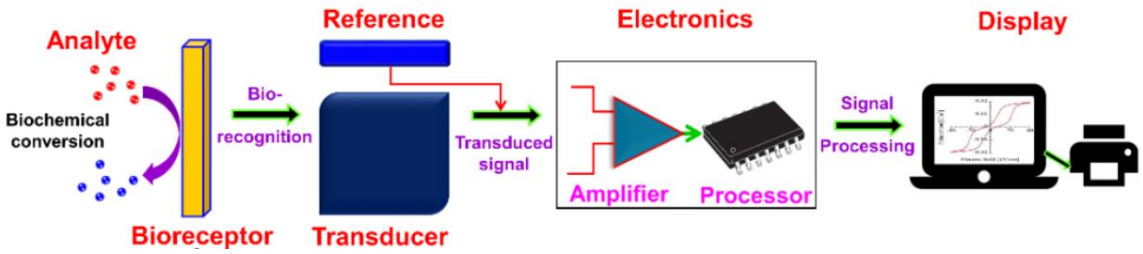

Figure 2. Overview of the necessary components of a biosensor (reprinted and edited from Naresh & Lee, 2021).[1]

In development, the sensitivity, selectivity, and reproducibility of a biosensor dictate its effectiveness.[3] The sensitivity is a measure of the limit of detection of an analyte, while the selectivity determines if a particular biosensor can consistently identify the analyte of interest. Reproducibility is a function of precision and accuracy, such that comparable results are obtained when a sample is run under similar conditions. Additional factors, such as response time, stability, and cost-efficiency also contribute to the practical commercial applications of a biosensor.[1]

While there is a great amount of diversity in biosensors, this analysis focuses on the optimization of an optical biosensor using surface-enhanced Raman spectroscopy. Due to its non-destructive sample analysis, molecular fingerprinting capabilities, and high sensitivity, SERS is an ideal technique for biosensor applications.[4] Past research in the Zhong research group has successfully utilized SERS analysis to detect the cancer biomarker carcinoembryonic antigen.[5] This analysis works to expand this platform for the eventual detection of SARS-CoV-2 on paper substrates. The basic components of the nanoprobe biosensor include a Raman reporter which shows a characteristic Raman shift upon the administration of photon, and an antibody which selectively binds to the antigen

of interest.[5] These two components are conjugated with nanoparticles, or clusters of metal atoms with a radius ranging from a couple nanometers to hundreds of nanometers, to ensure high intensity Raman scattering.[6]

1.2 Surface-enhanced Raman Spectroscopy Overview

SERS is a sensitive spectroscopic technique that can significantly enhance the detection capabilities of Raman scattering by dissolving molecules onto surfaces.[7] Without any surface enhancement, Raman signals are often too weak for analytical applications. Raman scattering is achieved by administering an incident photon to a sample. The photon can then be absorbed, vibrationally excite a molecule and be re-emitted at a new frequency. Most scattered photons are re-emitted elastically through Rayleigh scattering. In Stokes scattering, the incident photon is absorbed by a molecule in its vibrational ground state, which relaxes to a higher vibrational state by absorbing some of the incident photon's energy. As a result, Stokes photons experience a red shift. In anti-Stokes scattering, the molecule begins in a vibrationally active state, and after excitation relaxes to the ground state. The emitted photon thus experiences a blue shift, as shown in Figure 3.[7]

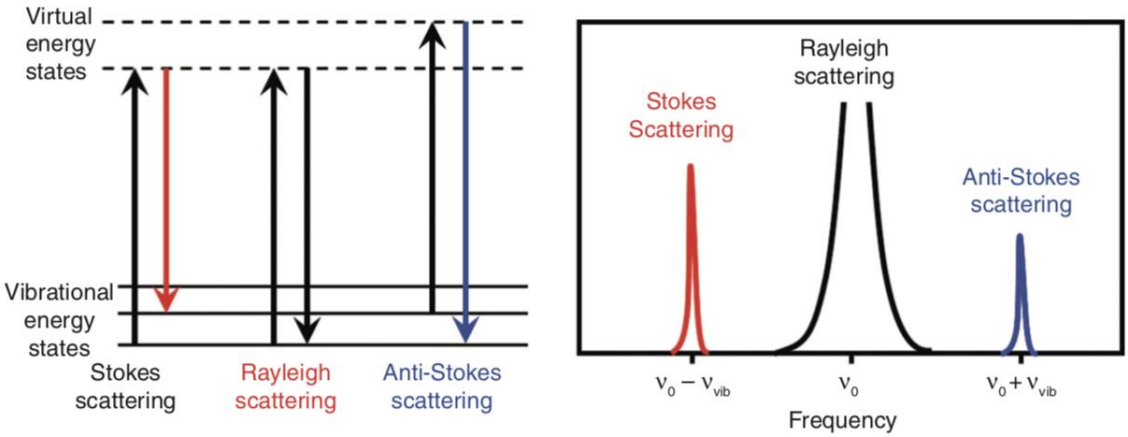

Figure 3. Overview of Raman scattering, including Rayleigh, Stokes, and anti-Stokes scattering (reprinted and edited from Kim et al., 2017).[8]

The first discovery of surface enhancement of Raman scattering occurred in the 1970s when Fleischmann and colleagues found that Raman scattering displayed an uncharacteristically strong response when a pyridine monolayer was absorbed onto a silver electrode.[9] Early theories argued that the increased surface area was responsible for the signal enhancement. Yet, work in the labs of Jeanmarie and Van Duyne and Albercht and Creighton suggested that a surface area effect could not summarize Fleischmann's findings.[10,11] Rather, Jeanmarie and Van Duyne asserted that these results occurred due to an enhancement of the electromagnetic field present within the metallic surface.[10] Albrecht and Creighton, however, claimed that a charge-transfer complex which formed between the silver and pyridine contributed to the enhancement.[11] From these two claims, researchers have developed the theories of electromagnetic and chemical SERS enhancement.[12] Today, it is generally accepted that both factors contribute to surface enhancement, with electromagnetic enhancement having a greater effect, particularly for metal surfaces.[4]

1.2.1 Electromagnetic Enhancement Mechanism

The electromagnetic enhancement mechanism can be broken down into local field enhancement and radiation enhancement. Local field enhancement occurs due to localized surface plasmon resonance, such that the Raman reporter experiences a local electric field ($E_{Loc}(\omega L)$), that is more powerful than the external electric field ($E(\omega L)$) because of its absorption on a surface.[12] Surface plasmon resonance (SPR) is a phenomenon commonly observed in metal nanoparticles. When exposed to electromagnetic radiation, the electrons in the conduction band of a metal oscillate around the particle surface, leading to a charge separation along the direction of the light.

The highest amplitude oscillation occurs at the surface plasmon resonance frequency, demonstrated in Figure 4.[13]

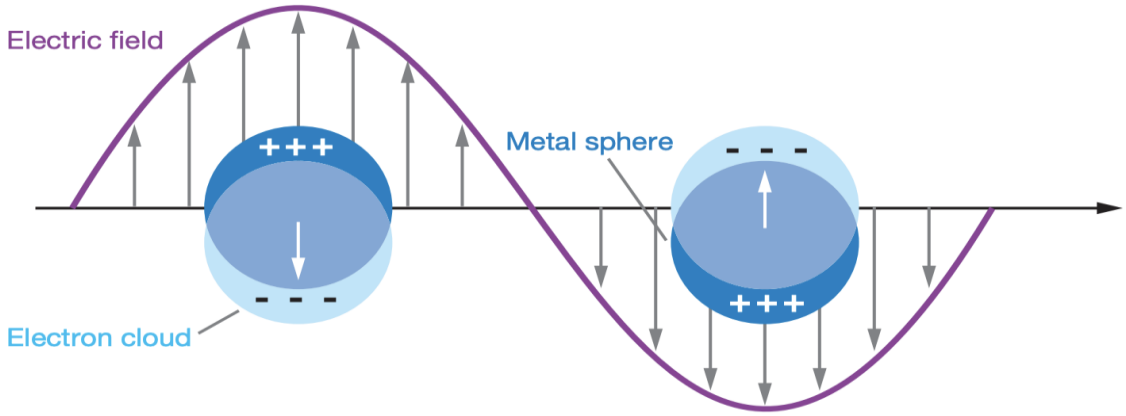

Figure 4. Schematic representation of the localized surface plasmon resonance band generated in metallic nanoparticles upon interaction with the electrical field of an incident light (reprinted and edited from Willets & Van Duyne, 2007).[14]

According to work from the physicist Gustav Mie the SPR wavelength and intensity is correlated with the metal type, size, shape, and dielectric environment, which all contribute to the amount of surface charge density.[15] Commonly, gold, copper, and silver nanoparticles are chosen for SERS analysis due to their high degree of surface plasmon resonance.[16] The local field enhancement is summarized through equation 1, where the Z term indicates that the laser is polarized along the Z axis.[12]

$$M^{Z}_{Loc(\omega_L)} = \frac{|E_{Loc}(\omega L)|^2}{|E(\omega L)|^2} \quad (1)$$

Radiation enhancement occurs due to the dependency of the power emitted from a dipole on the chemical environment.[12,17] When the chemical environment has interfaces present (i.e., is not homogenous), the electromagnetic field at the dipole is scattered and in part reflects backwards at the dipole position, impacting the power radiated.[12]

However, the electromagnetic contribution to SERS enhancement is commonly represented via the $|E|^4$ approximation, which is shown in equation 2,[18]

$$G_{SERS}^{Em} = \frac{|E_{Loc}(\omega L)|^4}{|E(\omega L)|} \quad (2)$$

where G_{SERS}^{Em} is the surface-enhancement because of the electromagnetic mechanism.

In general, the contribution from electromagnetic enhancement is approximated to be 10^8.[19] In "hotspots", or areas of sharpness or junctions in the nanoparticle surface, there is an even greater enhancement factor of 10^{10} due to higher localized surface plasmon resonance.[20] Figure 5 demonstrates the presence of a hot spot.

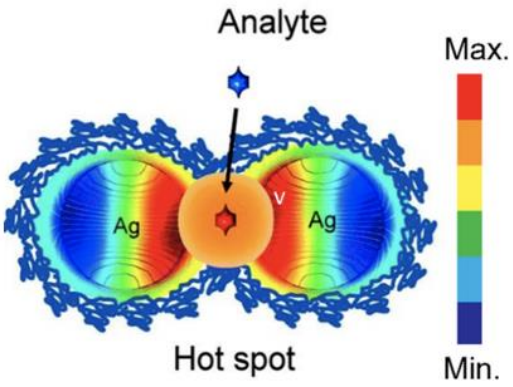

Figure 5. Representation of electromagnetic field enhancement at silver nanoparticle junctions through the development of a "hot-spot" (reprinted and edited from Radziuk & Moehwald, 2015).[21]

1.2.2 Chemical Enhancement Mechanism

Unlike electromagnetic enhancement, chemical enhancement occurs due to a change in the polarizability of the Raman reporter molecule due to interactions with the metal surface. Chemical enhancement is contingent on the Raman reporter molecule, and is considered a short-range effect, with nanoparticles and Raman reporter molecules required to be in close proximity to each other.[22] Generally, the enhancement factor from the chemical mechanism is estimated to range from 10^2 to 10^4.[23]

The absorption of a Raman reporter on a surface generally takes two forms. In physisorption, for instance, the molecule is absorbed because of Van der Waals interactions, and is not heavily modified. The change in enthalpy for this adsorption is generally believed to be lower than -25 kJ/mol. Conversely, if a molecule is absorbed in a chemisorption mechanism, a chemical bond is formed between the molecule and the surface, resulting in an enthalpy change lower than -40 kJ/mol.[24] These adsorptions both impact the vibrational cross-section of the molecule, and thus the SERS spectra. Mathematically, this enhancement is quantified by equation 3,

$$G_{SERS}^{Chem} = \frac{\sigma_k^{ads}}{\sigma_k^{free}} \quad (3)$$

where σ_k^{ads} is the surface dependent Raman cross section, σ_k^{free} is the free molecule Raman cross-section, and G_{SERS}^{Chem} is the surface enhancement due to the chemical mechanism.[12] Figure 6 includes a visual representation of chemisorption and physisorption of Raman molecules on a nanoparticle surface.

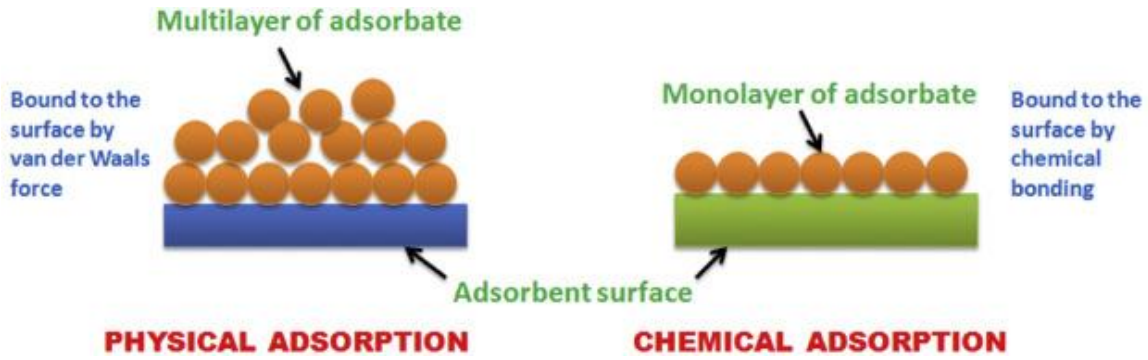

Figure 6. Schematic representation of physical and chemical absorption of Raman reporter molecules on surfaces (reprinted from Sarkar & Paul, 2016).[25]

The chemical enhancement mechanism can be explained through various mechanisms, but this discussion will focus on resonant charge transfer.[26] When the gap between Raman reporters' lowest unoccupied molecular orbital (LUMO) and highest

occupied molecular orbital (HOMO) are close to the Fermi level, or position of 50% occupancy of the metal, a metal-molecule charge transfer electronic state is achieved.[23] In resonant charge transfer, the allowed electronic transitions are enhanced when the laser source is in resonance with this state.[27] Figure 7 displays metal-molecule charge transfer.

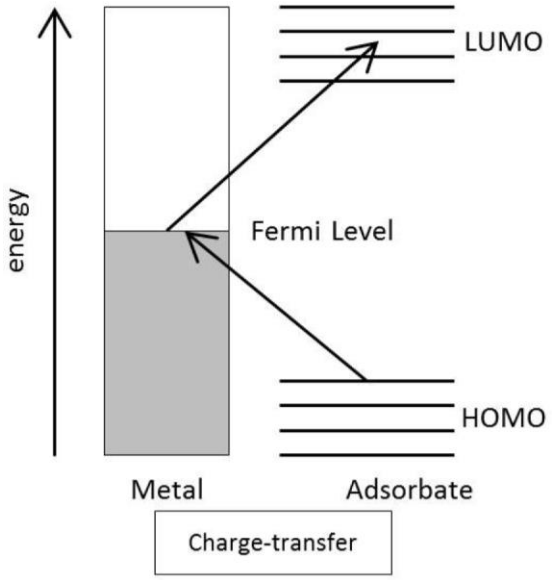

Figure 7. Schematic representation of the charge transfer resonance mechanism for SERS surface enhancement (reprinted and edited from Chu et al., 2017). [28]

1.3 Paper-based SERS Substrates

Beyond enhancements in SERS intensity due to the absorption of Raman reporter molecules on nanoparticle structures, advancements in paper-based SERS analysis have greatly expanded the practical applications of Raman scattering technologies.[29] The origin of paper-based SERS substrates can be traced back to 1984.[30] Unlike previously explored substrates, such as glass or silicon, paper provides enhanced flexibility, cost-efficiency, and ease of measurement.[31] Paper's cellulose composition additionally makes it biodegradable.[32]

1.3.1 Techniques for Nanoparticle Deposition on Paper

One early method for administering nanoparticles on paper substrates is the dip coating procedure, where paper substrates are dipped in nanoparticle solutions for a period of 24 hours and rinsed with water to remove residual nanoparticles not absorbed on the surface.[31] Nanoparticles can also be distributed on paper substrates by in-situ growth on paper, shown in Figure 8, where nanoparticles are grown by reducing metal ions in the pores of paper.[33] Advancements in inkjet-printing have also enabled the printing of both gold and silver nanoparticles on paper for use in sensors.[34]

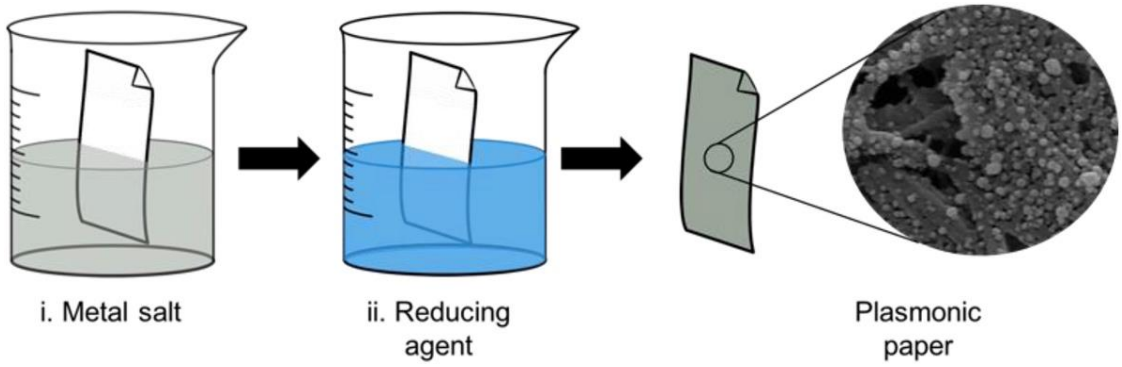

Figure 8. In-situ growth of nanoparticles in paper substrates (reprinted from Kim et al., 2015).[35]

An application of the *Lab-on-paper* methodology, developed by the Whitesides' group at Harvard University in 2007, will be utilized for nanoparticle distribution on paper substrates in this study. The Whitesides' method involves printing wax channels on paper substrates to serve as hydrophobic barriers for the solution of interest.[36] The channels are then heated to allow the wax to melt through the paper.[37] Solutions are allowed to flow through the channels via capillary action. A model of the groups' early channels can be seen in Figure 9.

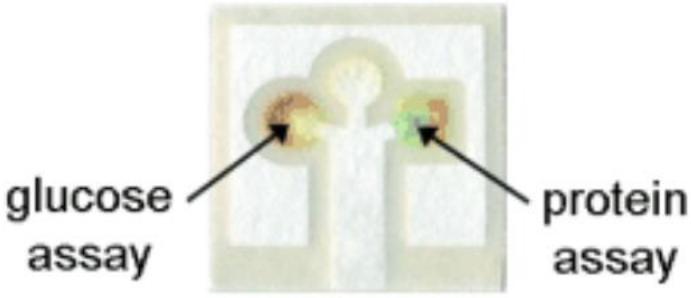

Figure 9. An early channel developed by the Whitesides' group at Harvard University for the paper-based detection of glucose and proteins (reprinted and edited from Martinez et al., 2007).[36]

One of the major critiques of paper-based SERS detection is its low reproducibility, and limit of detection.[38] As such, this study aims to optimize a methodology for using paper-based substrates for SERS analysis.

1.4 Objectives and Approach

This study seeks to optimize an experimental procedure in which gold nanoparticles, ranging in size from 30 nm to 60 nm, are conjugated with the Raman reporter 4-mercaptobenzoic acid (MBA) for paper-based SERS analysis. By determining the optimal solution preparation, transfer, and drying procedures, ongoing efforts are made to apply these parameters to the development of a biosensor for the detection of SARS-CoV-2.

The gold nanoparticles utilized in analysis are synthesized by means of seeded growth and nucleation.[39] MBA was chosen as a Raman reporter for this analysis due to its well characterized diagnostic Raman peaks at 1080 cm^{-1} and 1587 cm^{-1}. The 1587 cm^{-1} Raman shift occurs due to C-C ring stretching, and asymmetric C-H bending in plane, while the 1080 cm^{-1} band occurs due to breathing of the aromatic ring, and in plane symmetric C-H bending.[40] Figure 10 demonstrates the structure of MBA. It is important to note that MBA shows additional Raman bands depending on the solution pH.[40]

However, these bands will not be analyzed in this study due to their low intensity SERS responses. The conjugation of MBA with gold nanoparticles is achieved by means of the thiol (-SH) group on MBA. [40]

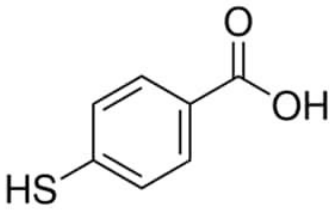

Figure 10. Chemical structure of the Raman reporter 4-mercaptobenzoic acid.

This paper specifically examines three factors in relation to dropwise administration of Au-MBA conjugates on wax-printed paper-based SERS channels. It determines the effect of the mode of solution drying (i.e., horizontal vs. vertical drying) on the SERS intensity of MBA. Figure 11 includes a schematic comparison of the horizontal and vertical drying procedures.

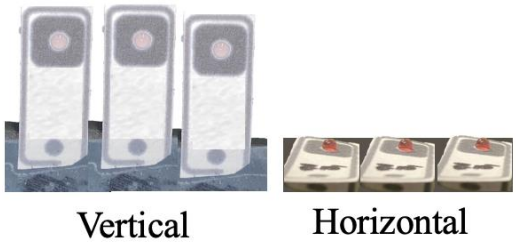

Figure 11. Photos showing the vertical and horizontal orientation drying procedures of gold nanoparticle solution on the wax-printed papers investigated in this work.

Additionally, it investigates whether the presence of a layer of candle wax backing on paper channels impacts the SERS spectra of MBA. Although wax backing may prevent sample loss from the backside of the channel, it is hypothesized that this backing will block two-sided evaporation during drying, leading to an accumulation of nanoparticles on the bottom of the channel. This non-uniform nanoparticle distribution is hypothesized to reduce the detection capabilities of SERS by limiting localized surface

plasmon resonance. This analysis will also characterize the limit of detection as a function of nanoparticle concentration. It will then determine what percentage of a theoretical nanoparticle monolayer is required to achieve a signal in SERS.

Once Au-MBA solution administration and drying procedures are optimized, a proof-of concept analysis can be conducted to evaluate the use of this platform as a biosensor for SARS-CoV-2 detection. To achieve this, a bioconjugation reaction between MBA, gold nanoparticles, and the SARS-CoV-2 Nucleocapsid (N-protein) antibody will occur.

2. EXPERIMENTAL PROCEDURE

2.1 Chemicals and Materials

The gold nanoparticle precursor gold (III) chloride trihydrate ($HAuC1_4 \bullet 3H_2O$, ≥99.9% trace metals basis) was obtained from Sigma Aldrich. Sodium acrylate (97%), the reducing/capping agent, was obtained from Aldrich. Sodium hydroxide (NaOH) pellets used in pH adjustment were purchased from VWR Life Science. The Raman reporter 4-Mercaptobenzoic acid (MBA, 99%) was obtained from Sigma Aldrich. The Cartridge-Free ColorQube Ink was used to wax print the SERS channels from the Xerox ColorQube 8580 Series. A Yamato Gravity Convection Oven DX 400 was used to heat the wax-printed paper substrates. The deionized water used in each experiment was purified from the Direct-Q3 Millipore Milli-Q system.

2.2 Nanoparticle Synthesis

The 30 nm nanoparticles utilized in SERS analysis were synthesized by colleagues in the Zhong research group following the established protocol.[41] 24 hours prior to synthesis, a 1.0 M solution of sodium acrylate was prepared and kept in a

refrigerator. An appropriate amount of the gold precursor ($HAuC1_4 \bullet 3H_2O$) was then dissolved in water with a magnetic stir. Through the addition of a 0.5 M NaOH solution, the solution pH was set to around 7. Sodium acrylate was added to the solution and mixed for nearly 72 hours. The progression of synthesis was monitored with Ultraviolet-visible spectroscopy (UV-vis). Transmission electron microscopy (TEM) was also used to verify the size of synthesized nanoparticles at completion.

To grow nanoparticles larger than 30 nm, the Zhong group protocol was followed.[41] The 30 nm gold nanoparticle seeds and the $HAuC1_4 \bullet 3H_2O$ solution were mixed, and pH adjusted to 7 with 0.5 M NaOH once again. The necessary amount of sodium acrylate was added to cap the nanoparticles at sizes of 30, 40, and 60 nm. The mixture was again stirred for approximately 72 hours. When the nanoparticles reached a consistent absorbance value the synthesis was finished, and TEM and UV-Vis analyses were conducted to verify nanoparticle size. Figure 12 demonstrates an overview of the synthesis process.

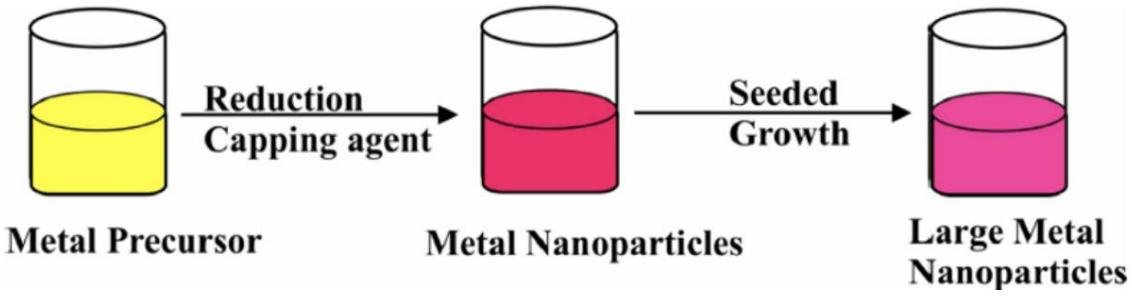

Figure 12. Schematic overview of the synthesis procedure for gold nanoparticles.

2.3 Au-MBA Conjugation

Conjugates between 30 nm, 40 nm, and 60 nm gold nanoparticles and MBA were obtained by dissolving the necessary amount of MBA to achieve a 5 mM solution of MBA in distilled water. A 1 M NaOH solution was added to the MBA until a pH ranging

from 7-8 was achieved and all the MBA was dissolved in water. The 5 mM MBA solution was then diluted with distilled water to achieve a 1 mM solution of MBA. The nanoparticles were mixed with MBA at a ratio of 1 mL of gold nanoparticles to 5 μL of 1 mM MBA and placed on the shaker overnight.

2.4 SERS Paper Substrate Preparation

SERS paper channels were developed on Microsoft Word, using a commercial silicon SERS plate as a basis for the size and shape parameters of the channels. The paper-based channels were wax printed on Whatman No. 1 Qualitative filter paper from Cytiva, using a Xerox ColorQube 8580. Figure 12 shows a sample of the printed channels. The preparation of SERS paper substrates will be further discussed in future paper.

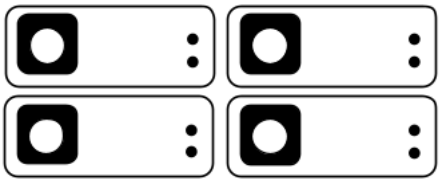

Figure 13. Illustration of the wax-printed paper wells/channels used for SERS analysis.

2.5 Instrumentation

2.5.1 Ultraviolet-visible Spectroscopy

A Hewlett-Packard 8453 spectrophotometer was used to generate the UV-vis spectra of Au-MBA and Au nanoparticle samples over a spectral range from 200 nm to 1100 nm. 4 mL BrandTech Polystyrene cuvettes were utilized for testing, with water as a blank. A schematic diagram of the UV-vis spectrophotometer can be found in Figure 14.

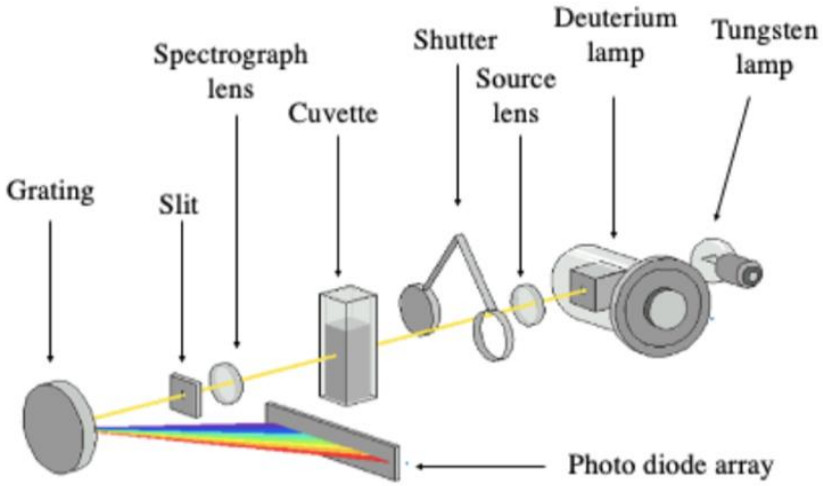

Figure 14. Schematic representation of the components of the UV-vis spectrophotometer.

UV-vis was utilized to validate nanoparticle size and conjugation with MBA. It is well documented in the literature that the surface plasmon band of gold nanoparticles smaller than 20 nm has a maximum wavelength of nearly 520 nm.[42] Past research in the Zhong group approximates that for each increase in nanoparticle diameter of 1 nm, the maximum wavelength is red shifted by around 0.7 nm, demonstrated in Figure 15.[43] It is additionally expected that the plasmon band will be red shifted after conjugation with MBA because of a change in the solution dielectric environment.[44] Figure 16 includes a representation of the change in nanoparticle color as a result of size.

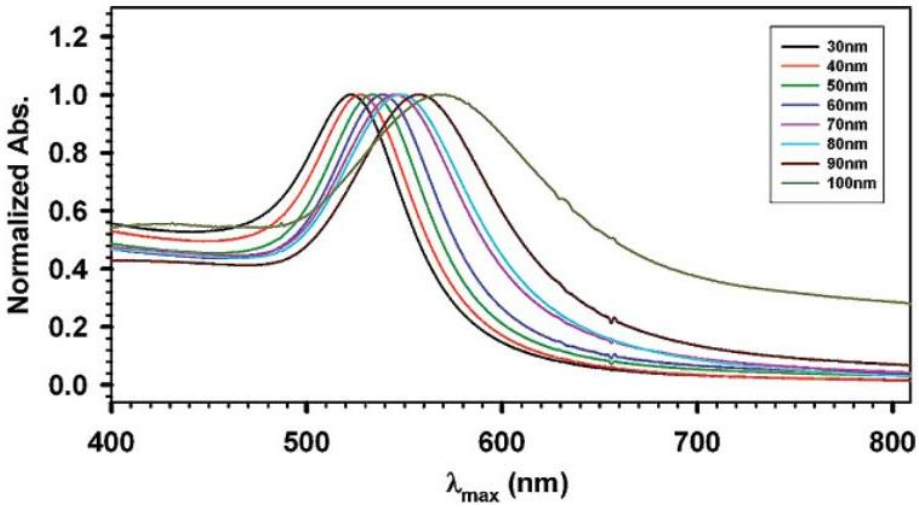

Figure 15. Normalized UV-Visible spectra of gold nanoparticles in solution as a function of nanoparticle size (reprinted from Njoki et al., 2007).[43]

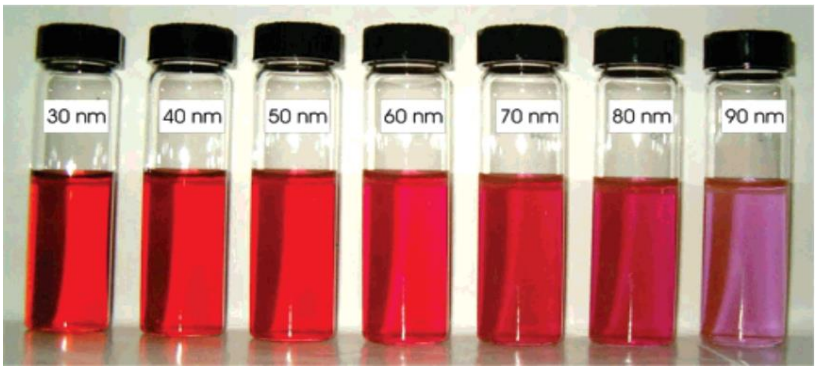

Figure 16. Photos showing the gold nanoparticles' color as a function of particle size (reprinted from Njoki et al., 2007).[43]

2.5.2 Transmission Electron Microscopy

TEM analysis of nanoparticle size was conducted by colleagues in the Zhong group. Nanoparticle images were generated with TEM by passing a thin beam of electrons through samples of the nanoparticle solutions. The electrons either scattered as they hit the nanoparticles or passed by the sample to a florescence screen at the bottom of the microscope, shown in Figure 17. [45] The electrons that hit the fluorescence screen generated the TEM image. [45]

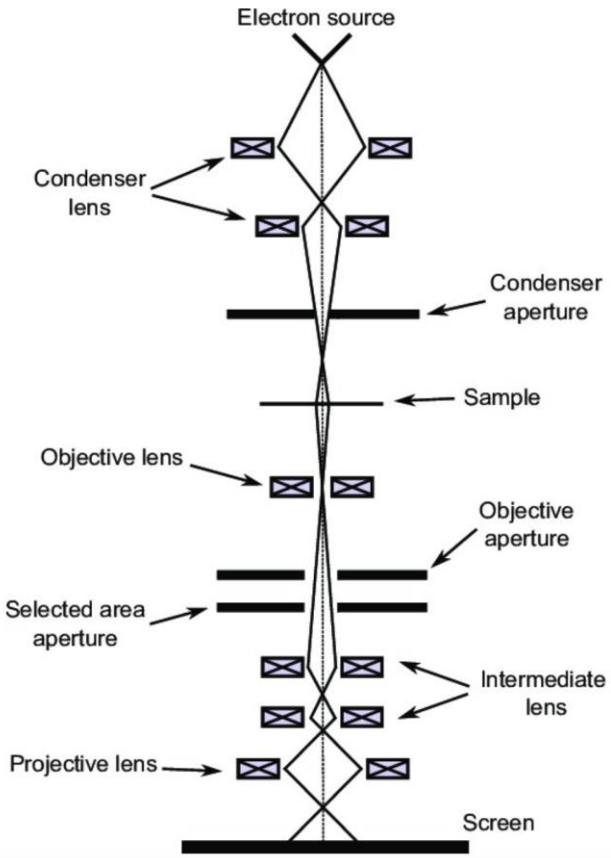

Figure 17. Schematic diagram of the components of a transmission electron microscope (reprinted from Marturi, 2013).[46]

The Corel Draw program was used to outline the scanned nanoparticles and ImageJ was used to correlate the number of pixels in a nanoparticle with its size.

2.5.3 Raman Spectroscopy

The Hamamatsu Raman spectrophotometer (serial number: 820OC103) was used for Raman data collection over a range of 0 to 2500 cm^{-1}. This instrument has an integration time of 1000 ms, and a laser with a wavelength of 785 nm. The maximum power output of the laser is 80 mW. A commercial silicon plate was utilized for calibration. Figure 18 displays the position of the paper-based SERS substrates in the Raman spectrophotometer for data collection.

Figure 18. Photo showing a paper-based SERS substrate in the Raman spectrometer for data collection.

2.6 Data Analysis

Excel and OriginPro were used for data analysis. The Peak Analyzer function on OriginPro was utilized for baseline correction to find the peak intensity.

3. RESULTS AND DISCUSSION

3.1 Nanoparticle Size Characterizations using UV-vis and TEM

Nanoparticle size was indirectly verified with UV-vis spectroscopy. Figure 19 includes a plot of the 30, 40, and 60 nm gold nanoparticle solutions' normalized UV-vis spectra. The 30 nm particles showed a maximum absorbance at a wavelength of 523 nm, while the 40 nm gold nanoparticles showed a peak absorbance at a wavelength of 526 nm. The 60 nm nanoparticles displayed a peak absorbance at a wavelength of 534 nm. As predicted, the surface plasmon band was red shifted with increases in nanoparticle size, showing good agreement with the literature.[43] Peak broadening was also noted as nanoparticle size increased.

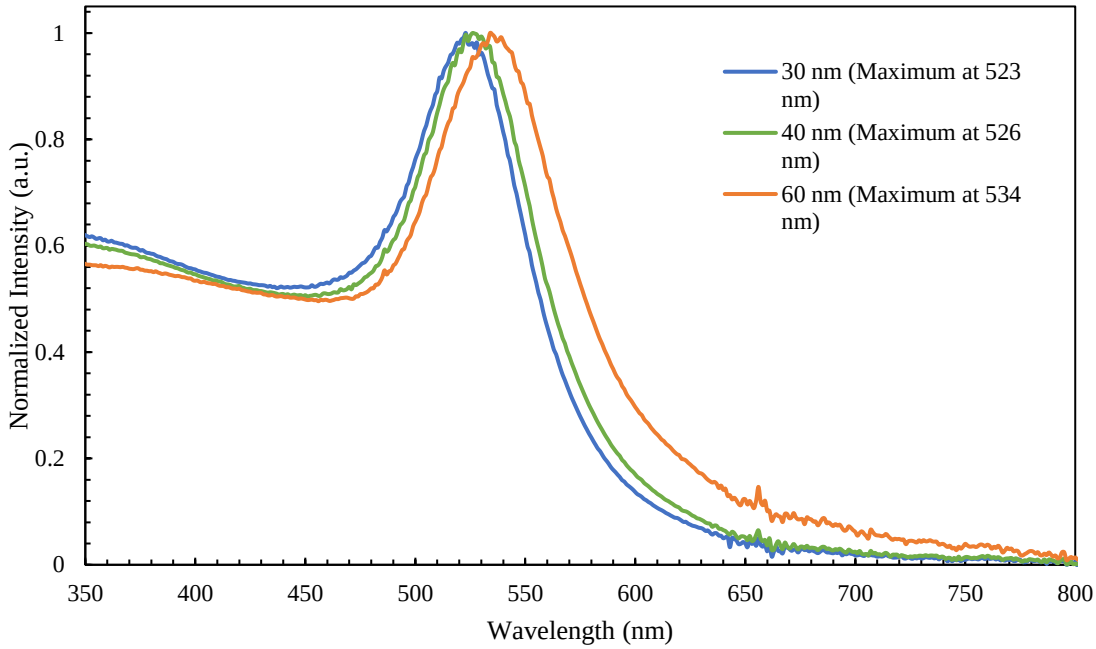

Figure 19. Nanoparticle size characterization with UV-visible spectroscopy.

TEM analysis provided a direct determination of nanoparticle size. Figure 20 displays images of 30 nm, 40 nm, and 60 nm nanoparticles under the same scale, as collected by collaborators in the Zhong research group.

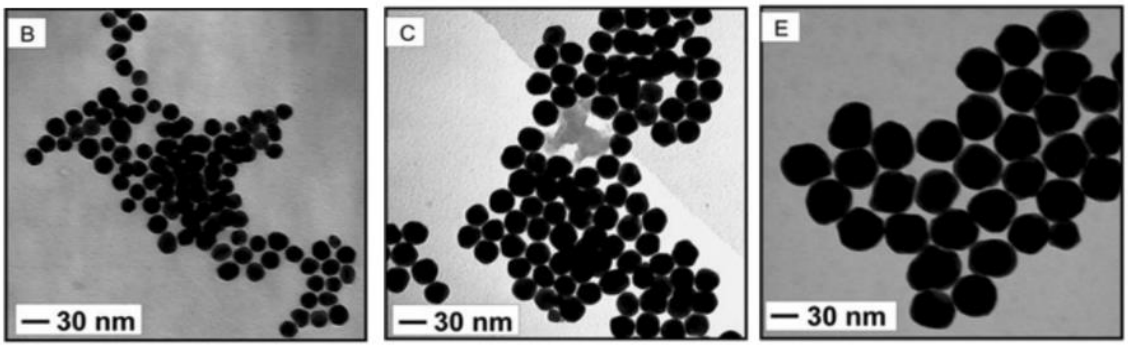

Figure 20. TEM micrographs of 30 nm (B), 40 nm (C), and 60 nm (E) gold nanoparticles (reprinted and edited from Njoki et al., 2010).[47]

3.2 Au-MBA Conjugate Characterization using UV-vis

UV-vis spectra for the 30 nm, 40 nm, and 60 nm Au-MBA conjugated solutions were collected. Figure 21 shows the UV-vis spectra of the 30 nm Au-MBA conjugate

solution, as compared with the 30 nm gold nanoparticle solution. As expected, the maximum peak of the 30 nm Au and 1 mM MBA solution was red shifted (524 nm) relative to the 30 nm gold solution (523 nm). This red shift has been well described in the literature as a result of a change in the dielectric properties of the gold nanoparticles after MBA conjugation.[48]

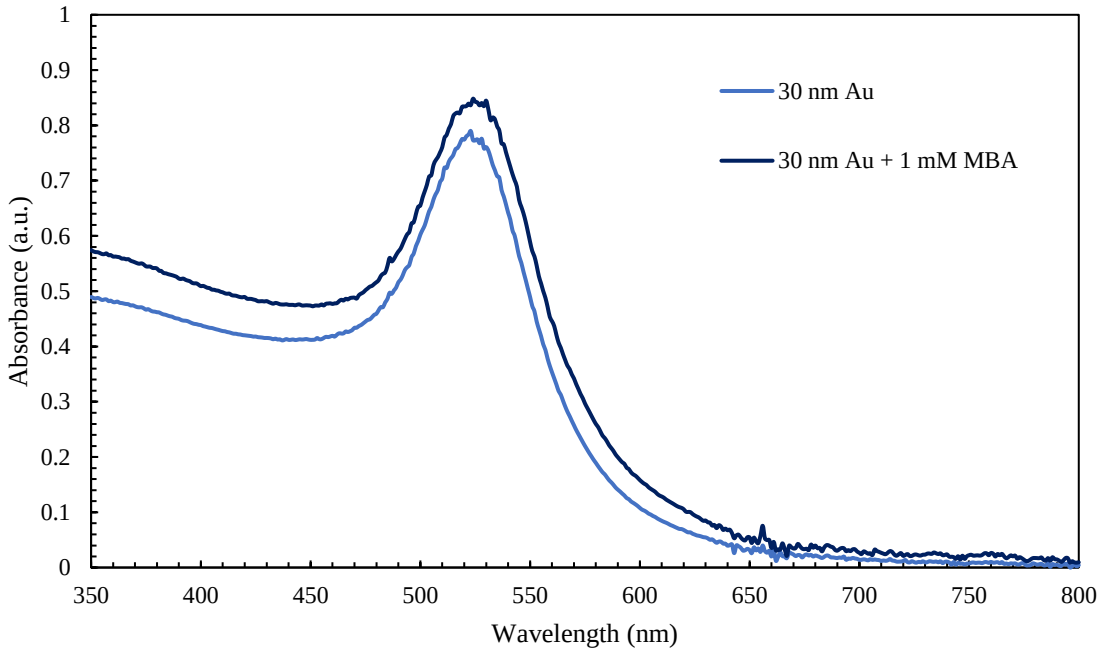

Figure 21. UV-vis spectra comparing the 30 nm Au and 30 nm Au-MBA.

Figure 22 demonstrates the UV-vis spectra for the 40 nm Au-MBA solution, relative to the 40 nm Au solution. Like the 30 nm Au-MBA conjugate solution, the 40 nm Au-MBA conjugated solution showed a red shift (528 nm) relative to the Au solution (526 nm). According to Mie theory, this result can be justified by a change in the dielectric environment after conjugation, which impacts the surface plasmon band.[48]

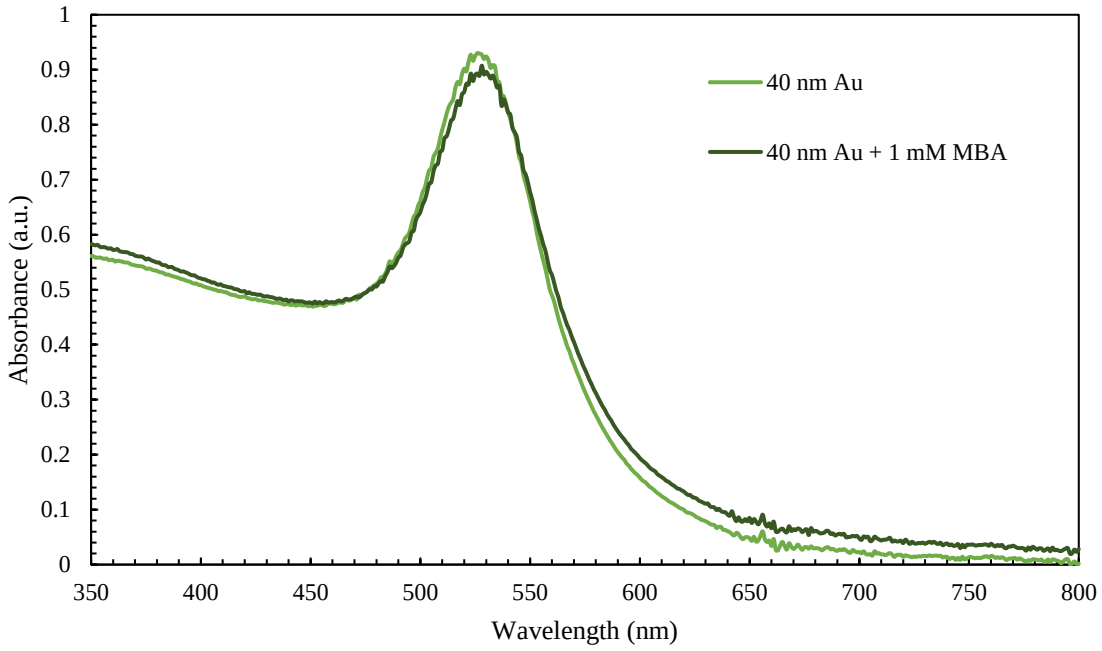

Figure 22. UV-vis spectra comparing 40 nm Au and 40 nm Au-MBA.

The UV-vis spectra for the 60 nm Au-MBA and 60 nm Au solutions are shown in Figure 23. Again, the Au-MBA spectrum showed a redshift after conjugation (537 nm).

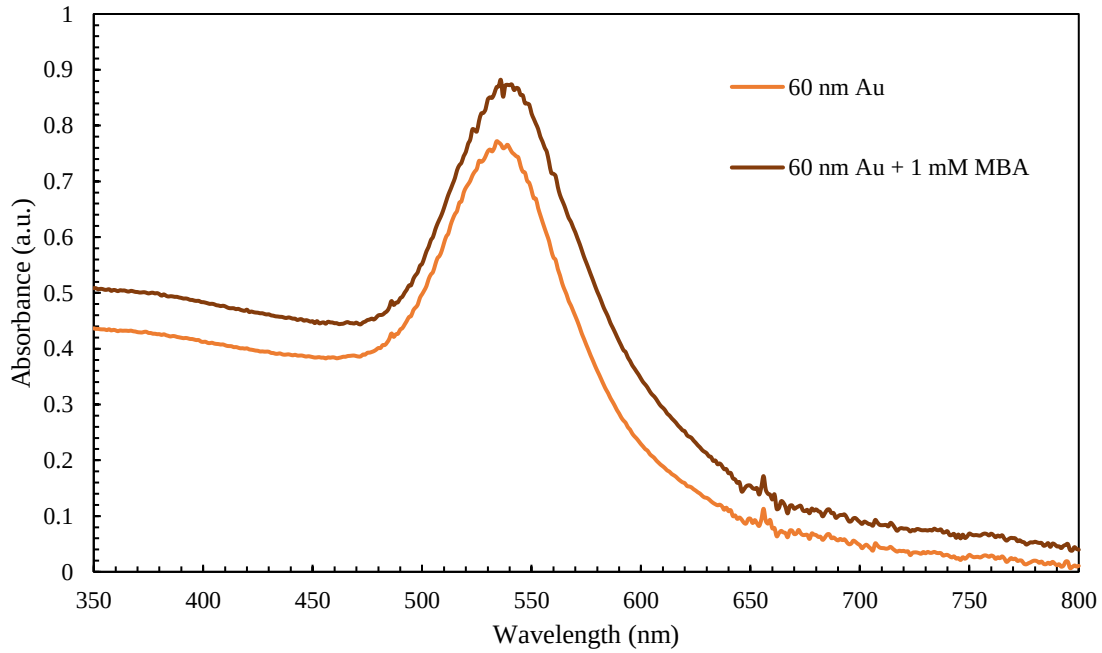

Figure 23. UV-vis spectra comparing the 60 nm Au and 60 nm Au-MBA.

3.3 SERS Paper Substrate Preparation

Wax channels were heated for time intervals ranging from one minute to five minutes and thirty seconds at an specific oven temperature. Figure 24 demonstrates the change in oven temperature due to its opening for approximately four seconds to insert the channels, as recorded from a calibrated multimeter. It took nearly one minute for the oven to return to temperature after opening. Thus, the channels were not heated at the set oven temperature for the entire duration that they were in the oven.

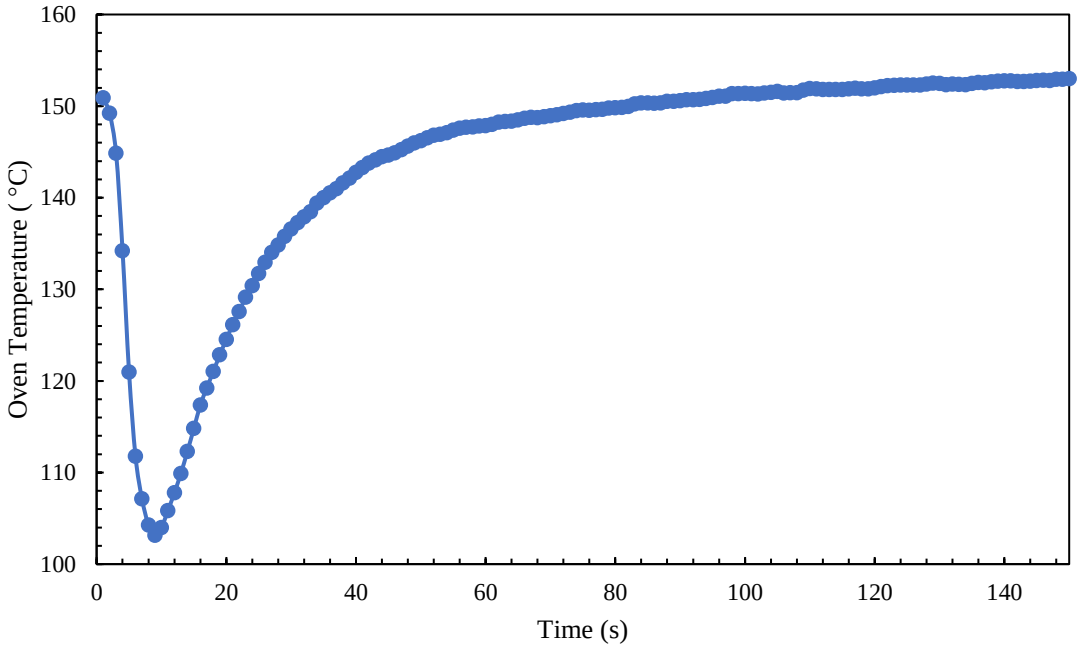

Figure 24. Plot of the oven temperature change after being open for a period of four seconds for sample placement in the oven.

Figure 25 shows the progression of wax melting on the backside of the wax-printed SERS channels as a function of time in the oven. Although various studies found a heating period of two minutes to be ideal, a qualitative analysis of heated channels revealed a heating time of two minutes and forty-five seconds to be an optimal duration for this study to prevent wax from melting into the circular well.[37] Yet, because it took the oven nearly forty-five seconds to reach temperature after opening, this value shows

good agreement with the literature. As such, all experiments were run on printed channels that were heated for this duration.

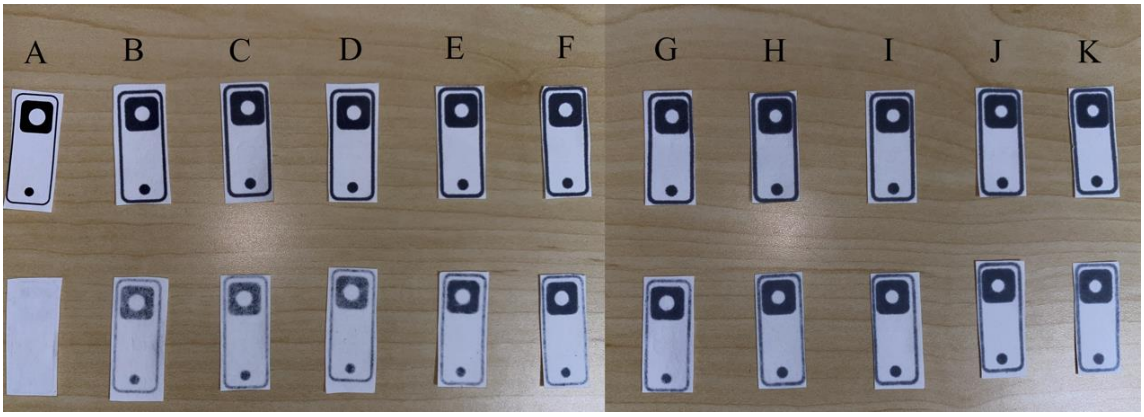

Figure 25. Photos showing the front (top) and back (bottom) of paper substrates after heating times of (A) unheated, (B) 1:00 min, (C) 1:30 min, (D) 2:00 min, (E) 2:30 min, (F) 3:00 min, (G) 3:30 min, (H) 4:00 min, (I) 4:30 min, (J) 5:00 min, (K) 5:30 min.

3.4 Comparison of Wax-Printed Paper SERS Substrates with and without Wax Backing Under Horizontal Orientation Drying Condition

The effectiveness of SERS analysis with and without wax backing on channels containing 60 nm Au-MBA conjugated solution was evaluated. This experiment focused on solution administration through dropwise horizontal drying procedures. Solution administration began with the dropping of 2.5 μL of 60 nm Au-MBA solution. A consistent 1.0 μL of solution was dropped on the same channel until the channel contained a maximum volume of 7.5 μL. Three replicates of each volume were collected. Figure 26 includes the average SERS spectra for channels without wax backing as a function of the amount of Au nanoparticles dropped on the channel. It was estimated that 2.3×10^{10} Au nanoparticles were present in each mL of solution administered. The SERS spectra is scaled to analyze the two diagnostic Raman peaks for MBA at 1080 cm^{-1} and 1587 cm^{-1}.

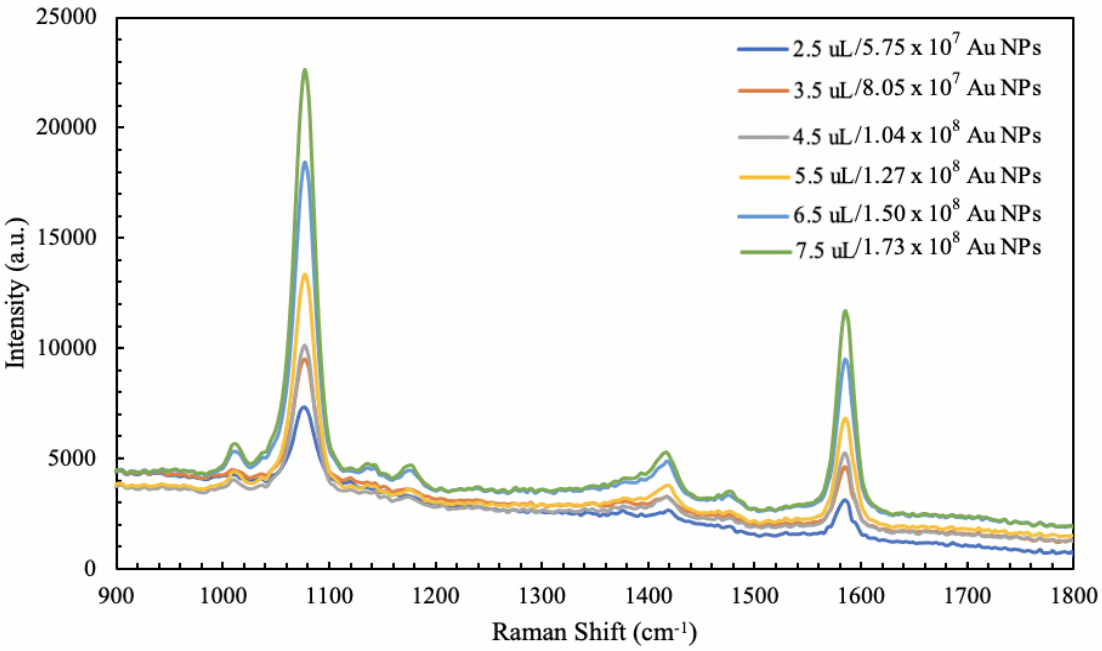

Figure 26. Average Raman spectra of three no-wax backed SERS substrates as a function of the dropped volume in terms of the nanoparticle amount.

Figure 27 contains the average Raman spectra for channels containing wax backing as a function of dropped volume, and therefore nanoparticle amount.

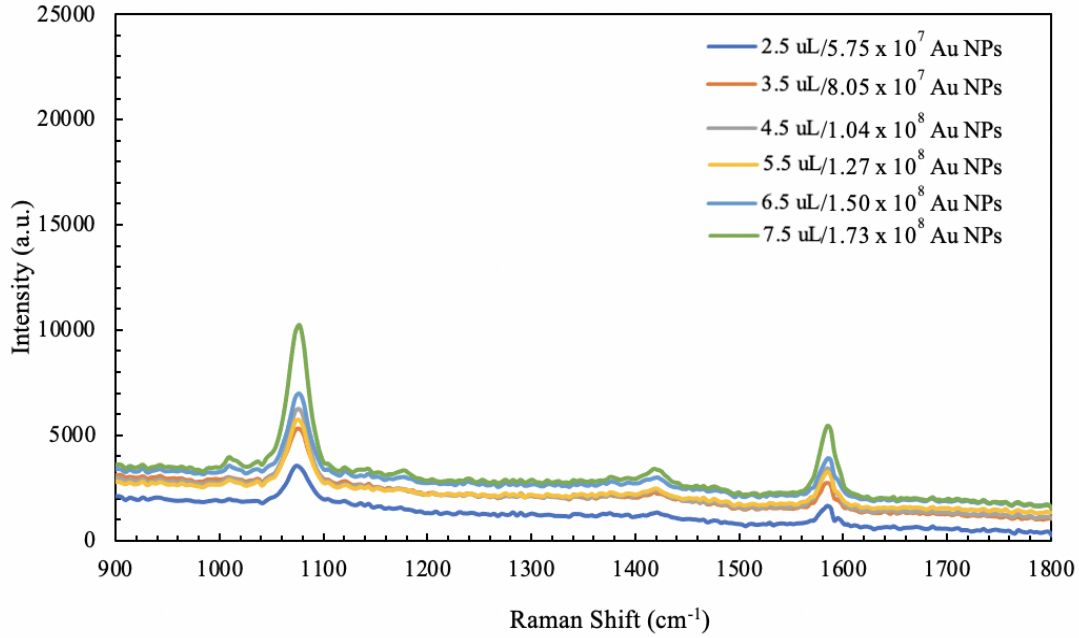

Figure 27. Average Raman spectra of three wax backed SERS substrates as a function of the dropped volume in terms of the nanoparticle amount.

One important finding from both the channels with and without wax is that the SERS intensity significantly increases with increasing amounts of nanoparticles. This result is in direct alignment with enhanced surface plasmon resonance.[48] Figure 28 plots the average maximum intensity at the diagnostic 1080 cm^{-1} Raman peak for MBA after baseline correction with OriginPro. This result demonstrates that the channels without wax backing are more sensitive, with a slope of 0.0001 a.u. NP^{-1}, as compared with a slope of 2 x 10^{-5} a.u. NP^{-1} for wax backed channels. This suggests that channels without wax backing are five times more sensitive than wax-backed channels when dried horizontally. The no-wax backed channels also show enhanced linearity (R^2 = .9507) when compared to wax backed channels (R^2 = .8407).

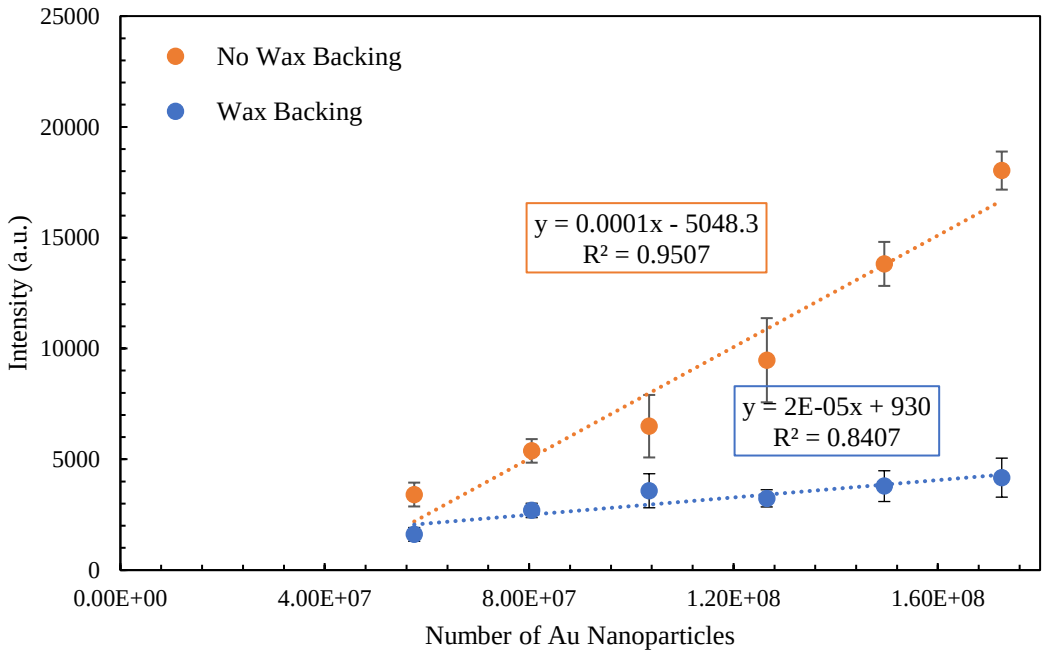

Figure 28. SERS peak intensity at the 1080 cm^{-1} Raman shift as a function of the number of gold nanoparticles in the no wax and wax backed SERS substrates after baseline correction with OriginPro.

Taken together, these findings indicate that for dropwise horizontal Au-MBA administration no-wax channels show enhanced sensitivity and linearity.

3.5 Nanoparticle-Coverage Dependence with SERS Substrates Prepared by Vertical Orientation Drying

Prior to investigating the difference between wax and no-wax backed channels in vertical drying, a Raman spectrum for vertically dried 30 nm Au-MBA no-wax backed channels was developed. This experiment aimed to determine if a substantial volume of solution could be dried vertically without sample loss due to dripping from the testing area. Three replicates were tested, each containing a maximum volume of 6.5 µL, with 1.0 µL dropped consistently starting from an initial volume of 0.5 µL. For 30 nm gold nanoparticles, the number of nanoparticles present in each mL of solution was approximated to be 1.5 x 10^{11} nanoparticles. Figure 29 shows the average Raman spectra for 30 nm Au-MBA conjugated channels without wax backing that were dried vertically after dropwise addition of solution.

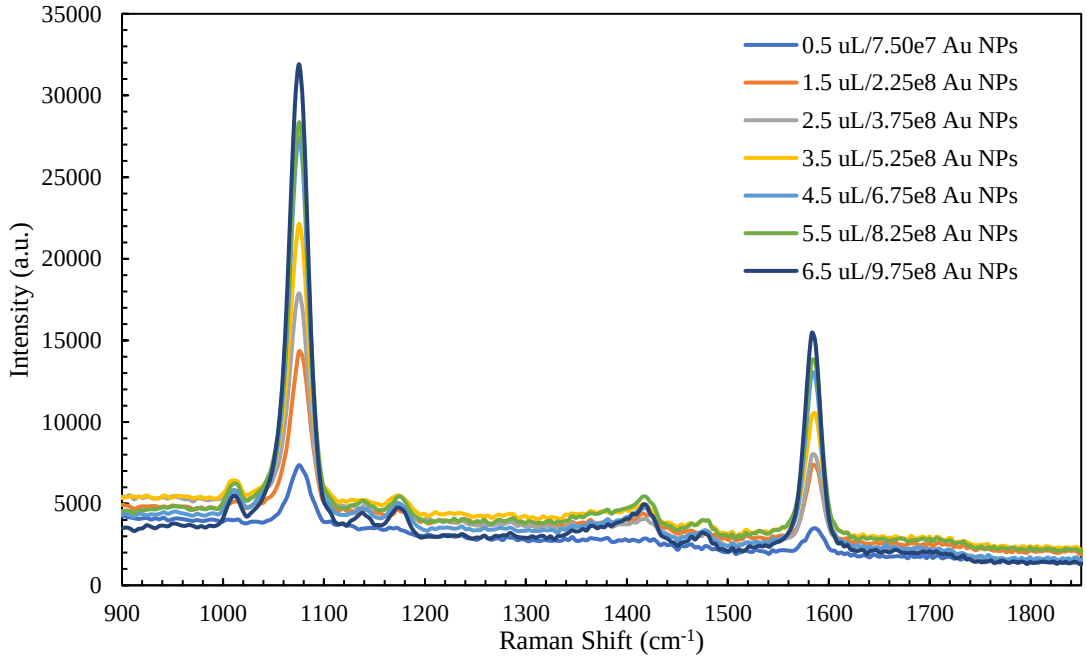

Figure 29. SERS spectra for 30 nm Au-MBA no-wax backed channels after vertical drying, as a function of nanoparticle amount.

A plot of the average maximum intensity at the 1080 cm^{-1} Raman peak after baseline correction can be seen in Figure 30. As expected, as the concentration of 30 nm Au nanoparticles increased, the SERS intensity increased linearly (R^2 = .9765) because of increased surface plasmon resonance.[48] This experiment demonstrated that large volumes of Au-MBA can be dried in a vertically without sample loss and with good sensitivity.

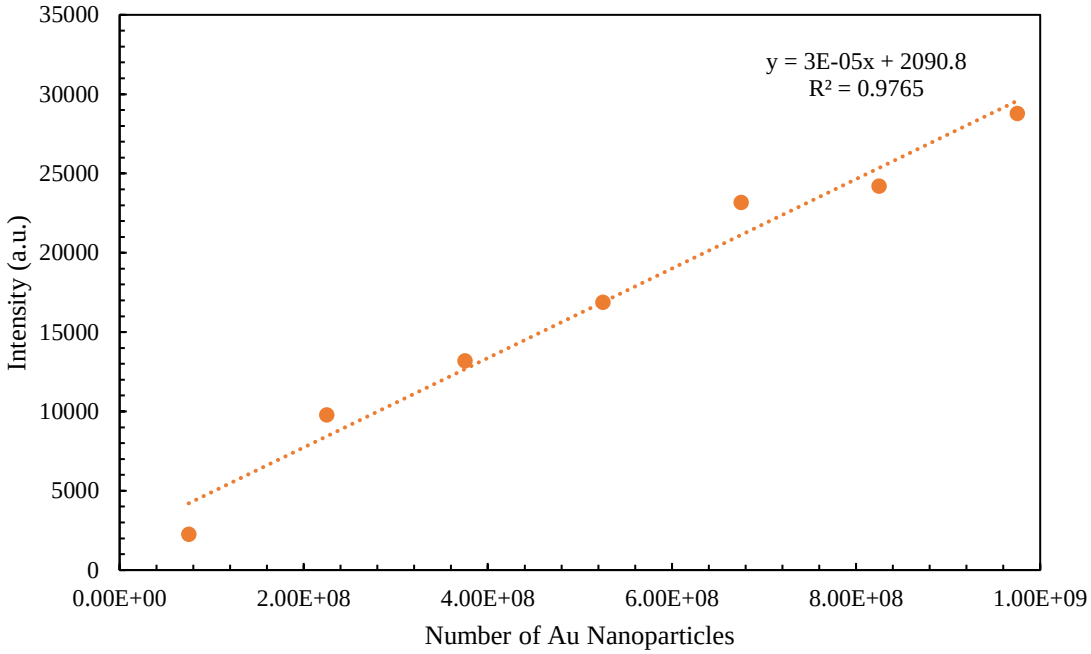

Figure 30. Plot of the SERS peak (at 1080 cm^{-1}) intensity vs. the number of Au nanoparticles for 30 nm Au-MBA in the no-wax backed substrates after baseline correction with OriginPro.

3.6 Comparison of Wax-Printed Paper SERS Substrates with and without Wax Backing Prepared under Vertical Orientation Drying Condition

To further explore the role of wax backing, solutions of 30 nm, 40 nm, and 60 nm Au-MBA conjugates were analyzed with wax and no wax backing.

3.6.1 30 nm Au-MBA

Figures 31 and 32 contain the Raman spectra for 30 nm Au-MBA solutions administered in a dropwise fashion with and without wax backing.

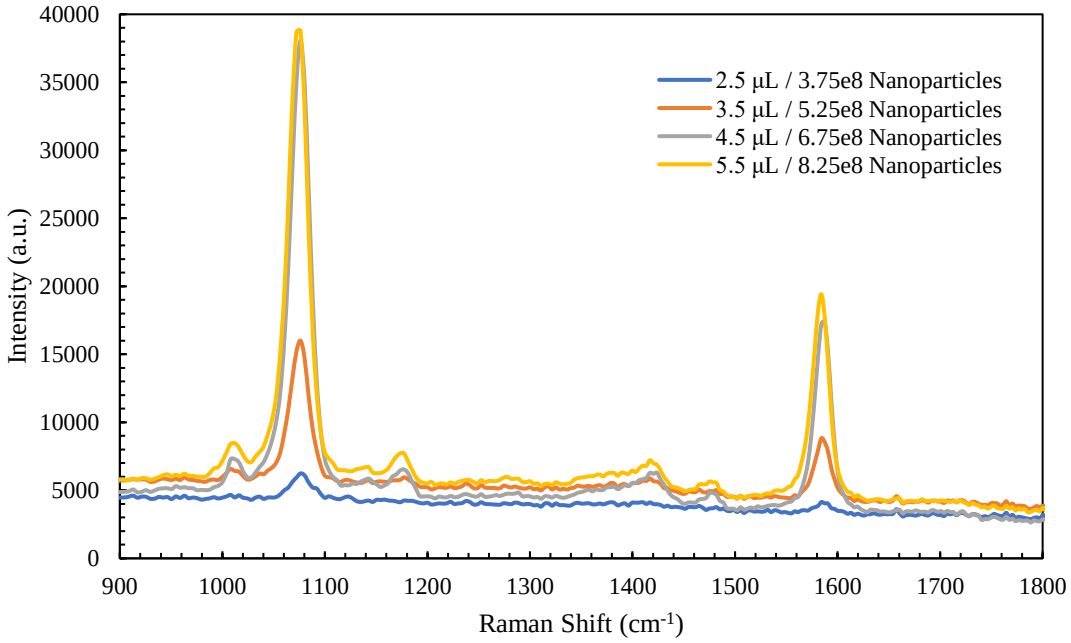

Figure 31. SERS spectra for 30 nm Au-MBA solution dropped on channels without wax backing and following vertical drying procedures.

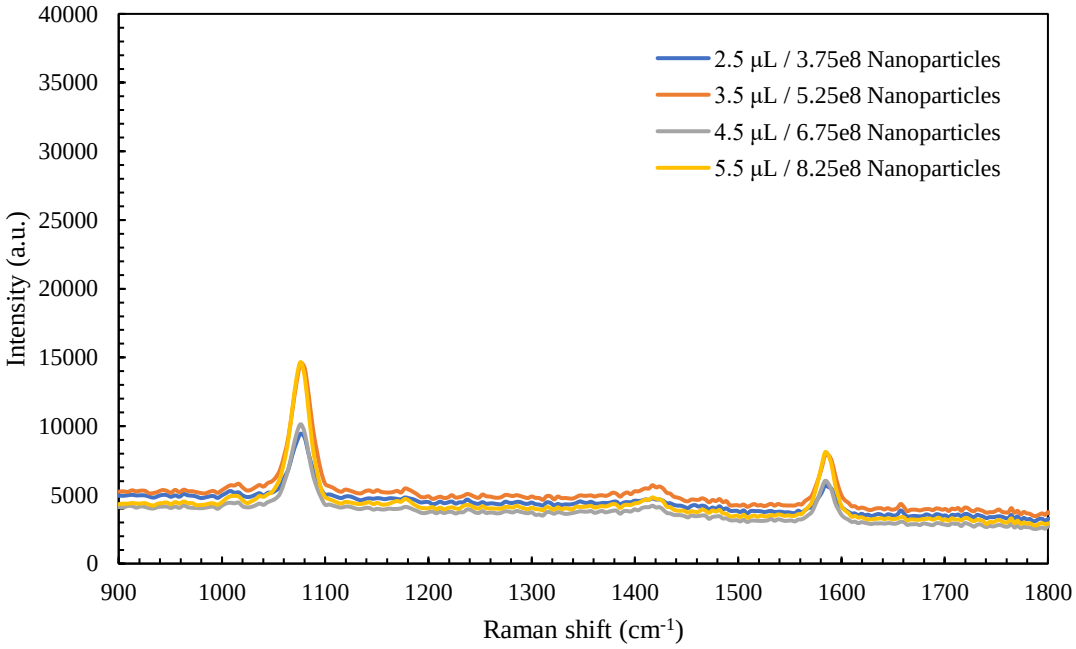

Figure 32. SERS spectra for 30 nm Au-MBA solution dropped on channels with wax backing and following vertical drying procedures.

After baseline correction with OriginPro, Figure 33 plots the maximum Raman intensity as a function of nanoparticle amount at the 1080 cm^{-1} peak. This analysis again

reveals that channels without wax backing show greater sensitivity, with a slope of 8.0 x 10^{-5} a.u. NP^{-1} as compared to wax backed channels with a slope of 9.0 x 10^{-6} a.u. NP^{-1}. This suggests that channels without wax backing show nearly eight times the sensitivity of wax backed channels. The channels without backing also showed significantly higher linearity (R^2 = .9043) as compared to wax backed channels (R^2 = .4456).

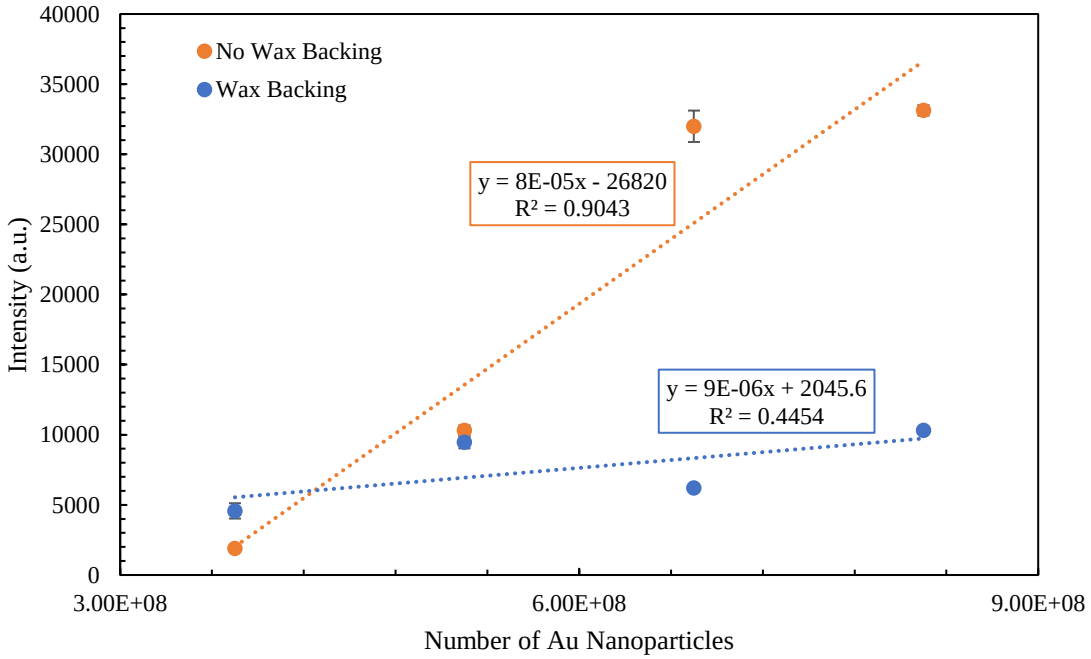

Figure 33. Plot of SERS peak (at 1080 cm^{-1}) intensity for 30 nm Au-MBA in no-wax and wax backed substrates after baseline correction with OriginPro.

3.6.2 40 nm Au-MBA

40 nm Au-MBA conjugates were additionally tested on channels with and without wax backing through dropwise administration beginning at 2.5 µL. The average amount of gold nanoparticles in each mL of solution was estimated to be 5.80 x 10^{10}. As such, the approximated maximum amount of Au nanoparticles dropped was 3.19 x 10^{8} nanoparticles. Figures 34 and 35 include the average Raman spectra of no-wax and wax backed channels, respectively.

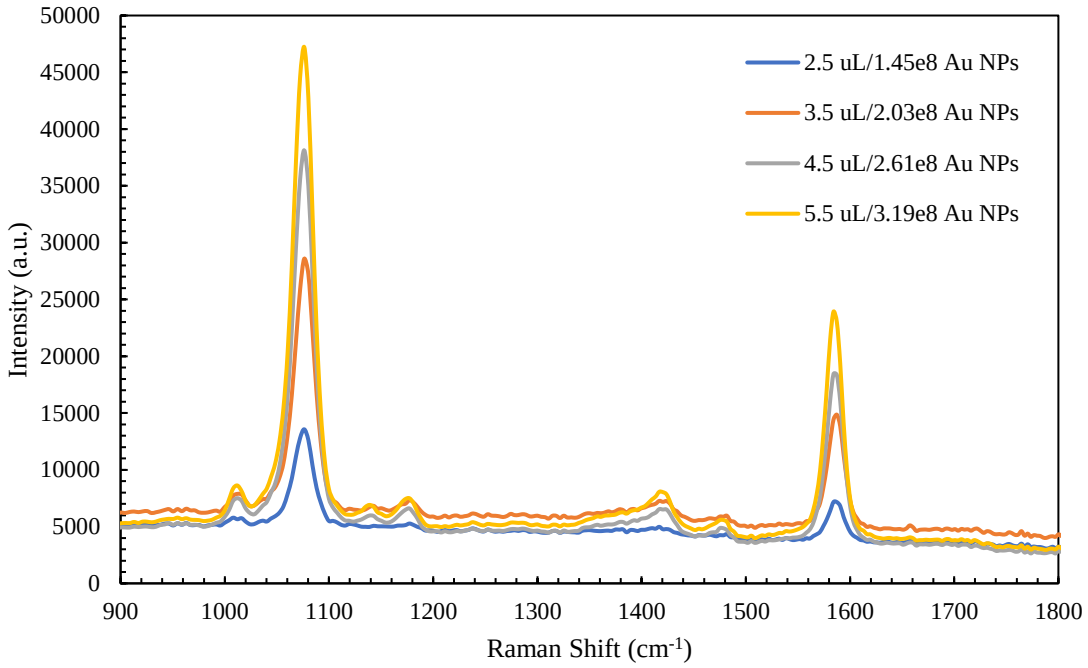

Figure 34. SERS spectra for 40 nm Au-MBA solution dropped on channels without wax backing and following vertical drying procedures.

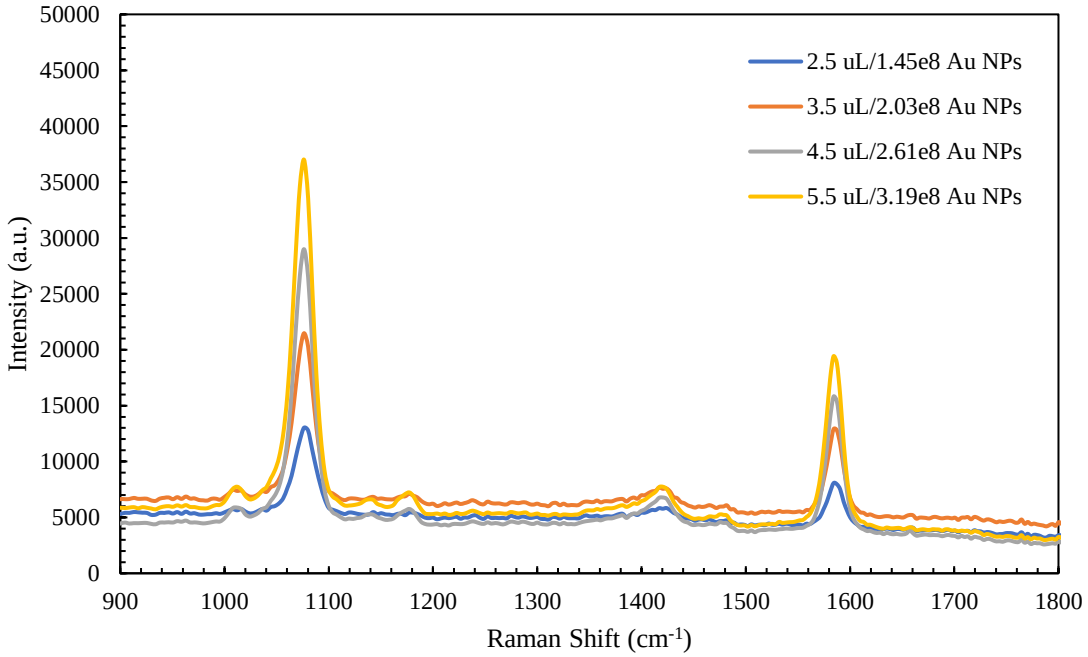

Figure 35. SERS spectra for 40 nm Au-MBA solution dropped on channels with wax backing and following vertical drying procedures.

Again, this data is in alignment with increasing Raman intensity as a function of increased surface plasmon resonance with more gold nanoparticles administered. Figure

36 contains a plot of the average maximum intensity at the 1080 cm^{-1} Raman peak after baseline correction. Unlike the 30 nm Au-MBA conjugates, both the no-wax (R^2 = .9867) and wax (R^2 = .9965) backing channels showed strong linearity. This could suggest some experimental errors (i.e., improper channel placement in the Raman) leading to the poor linearity of the 30 nm Au-MBA wax backed channels. Yet, this analysis revealed a consistent trend in sensitivity, with no-wax backed channels showing twice the sensitivity (m = 0.0002 a.u. NP^{-1}) as the wax backed channels (m = 0.0001 a.u. NP^{-1}).

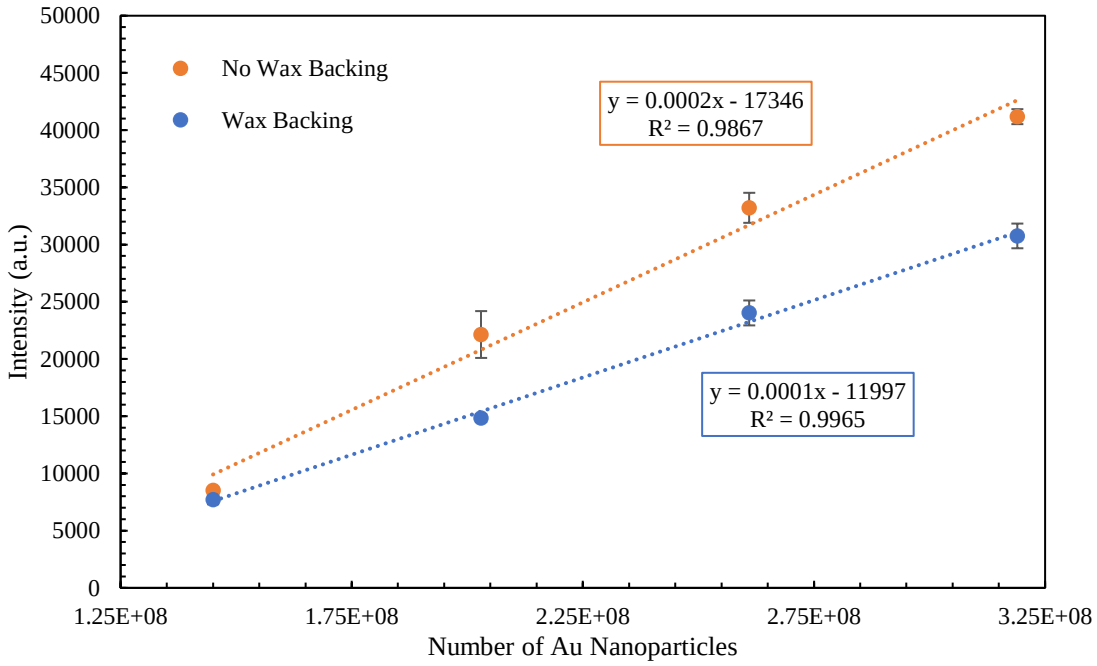

Figure 36. Plot of SERS peak intensity for 40 nm Au-MBA no-wax and wax backed channels at the 1080 cm^{-1} peak after baseline correction with OriginPro.

3.6.3 60 nm Au-MBA

The final size analyzed for a wax and no-wax backing comparison via vertical drying was the 60 nm Au-MBA solution. The maximum concentration of Au nanoparticles distributed was 1.27 x 10^8. Figures 37 and 38 include the baseline corrected Raman spectra for channels with and without wax backing.

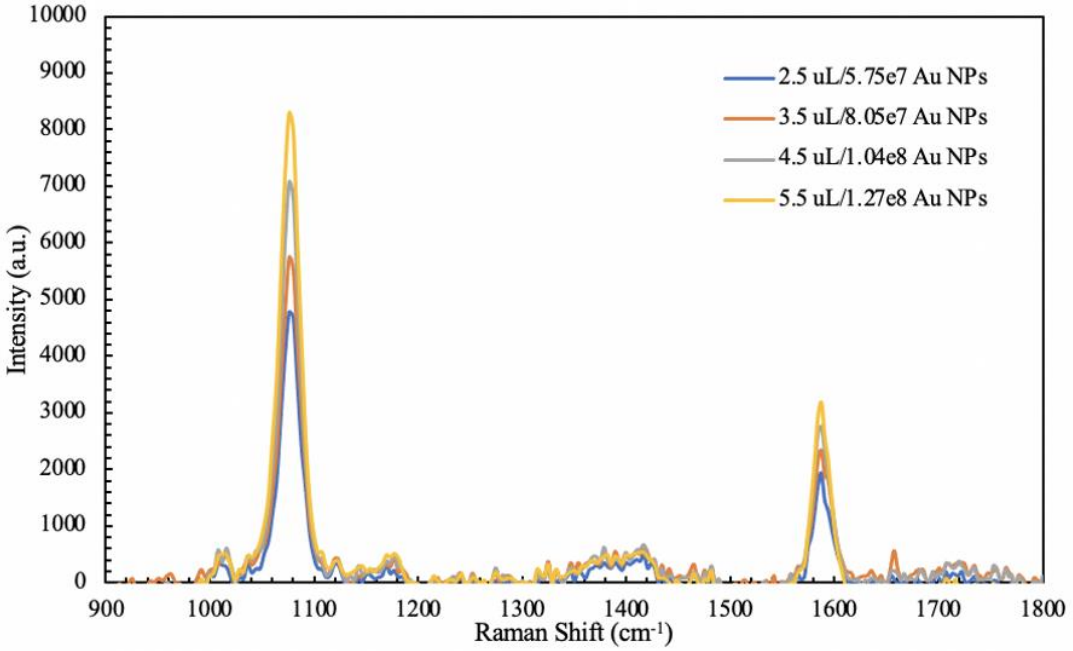

Figure 37. Baseline corrected SERS spectra of 60 nm Au-MBA solutions dried vertically with no wax backing.

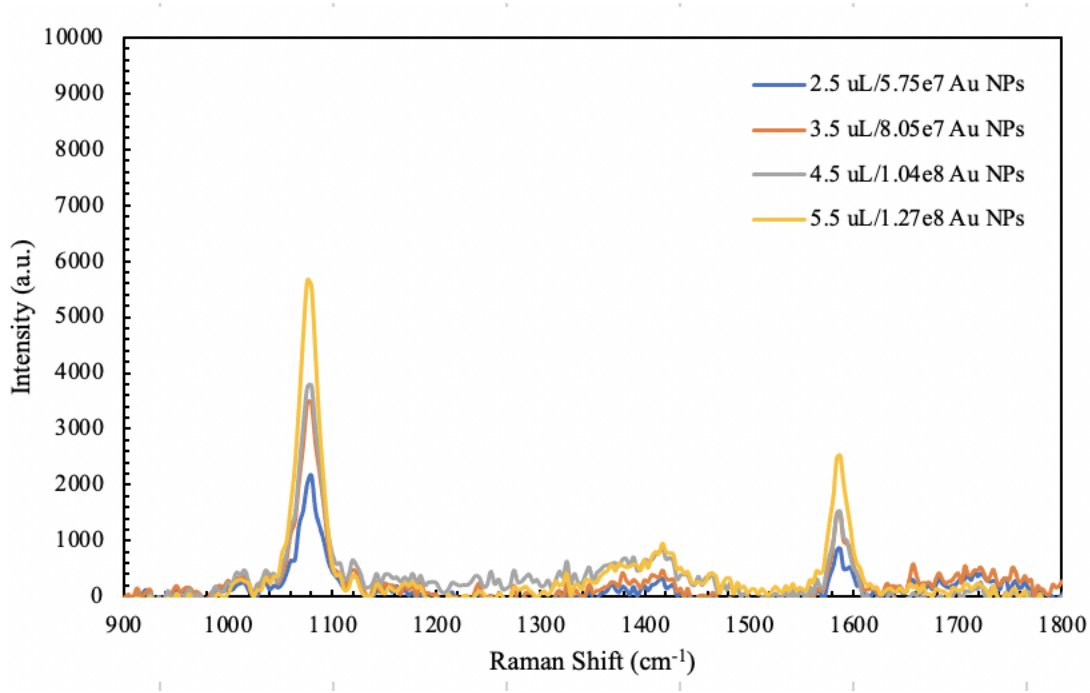

Figure 38. Baseline corrected SERS spectra of 60 nm Au-MBA solutions dried vertically with wax backing.

The average maximum Raman signal for the baseline corrected wax and no-wax channels at the 1080 cm^{-1} peak can be found in Figure 39. This data matches the trends

established with horizontal drying 60 nm Au-MBA, such that channels without backing have higher sensitivity (m = 7.0 x 10^{-5} a.u. NP^{-1}) and linearity (R^2 = .9441) than the wax backing channels (m = 3.0 x 10^{-5} a.u. NP^{-1}, R^2 = 0.8361). The no-wax channels show double the sensitivity of the wax backing channels, as observed for 40 nm NPs.

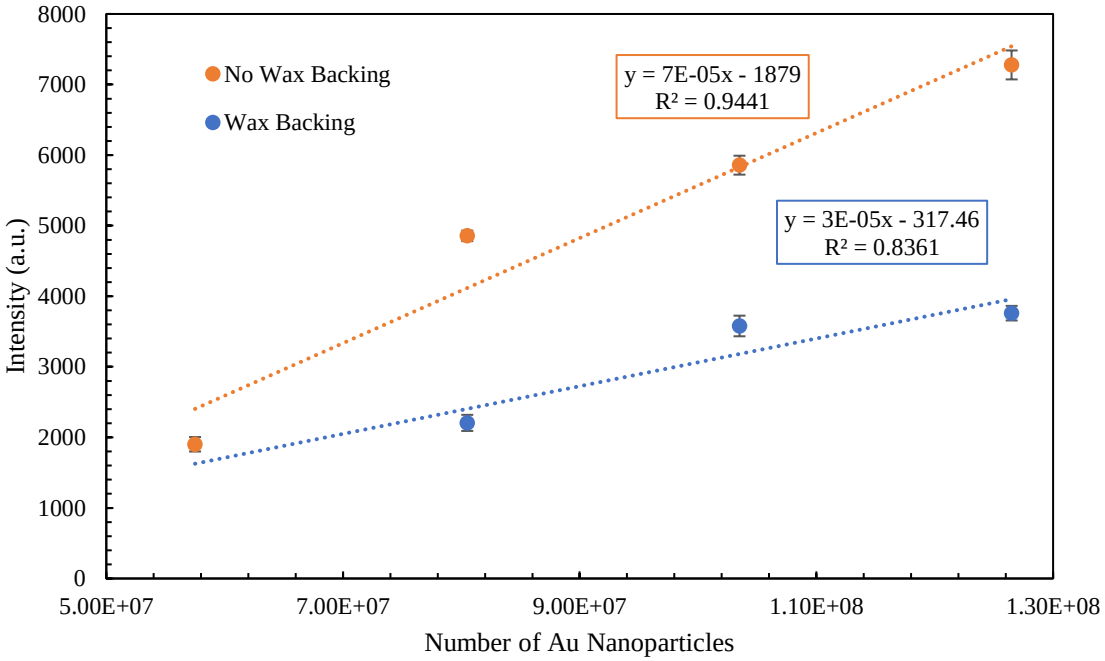

Figure 39. Plot of SERS intensity for 60 nm Au-MBA no-wax and wax backed substrates at the 1080 cm^{-1} peak after baseline correction with OriginPro.

Taken together, the wax backing analysis reveals that paper substrates without wax backing show greater linearity and sensitivity in SERS analysis at gold nanoparticle sizes of 30 nm, 40 nm, and 60 nm. It is believed that paper substrates without backing show enhanced SERS detection capabilities because of two-directional solution evaporation from the top and bottom of the channel. Conversely, in wax backed channels, the solution is only free to evaporate from the top side of the channel, leading to an accumulation of gold nanoparticles attached to paper fibers near the candle wax backing. With this accumulation of gold nanoparticles at the bottom of the channel the localized electric field is reduced.[13] It is also possible that the Raman laser collides with paper

fibers significantly more before reaching the nanoparticles in wax-backed channels, contributing further to the reduction in SERS sensitivity with wax backed channels. Figure 40 includes a schematic representation of this wax vs. no-wax backing hypothesis.

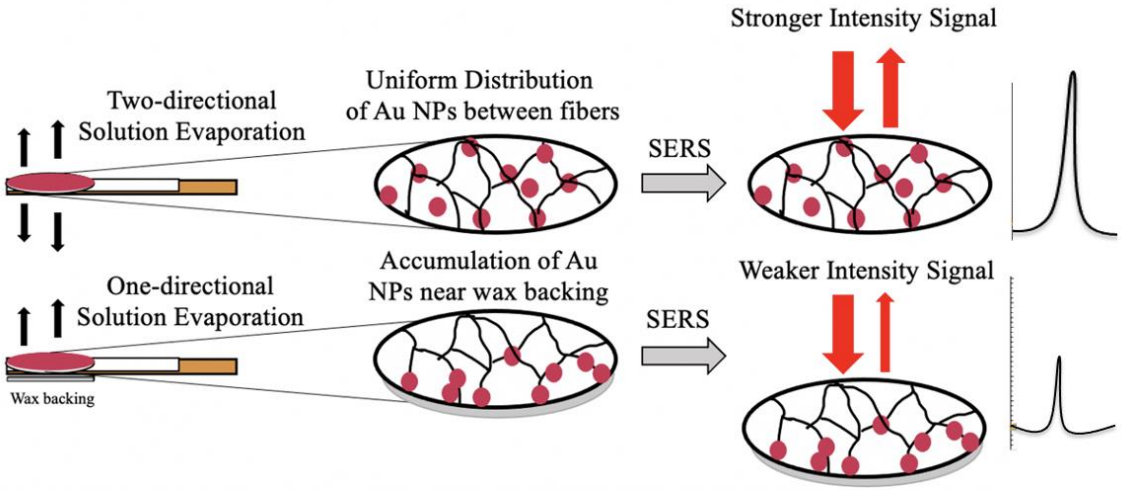

Figure 40. Schematic representation of the hypothesis for the nanoparticle dispersed paper substrates prepared by two different procedures.

This analysis also suggests that the mode of solution administration can contribute to SERS intensity, but more study is needed to directly compare vertical and horizontal drying procedures. Another facet of solution administration is dropwise addition. By administering solutions incrementally at low volumes via a dropwise addition mechanism, gold nanoparticles are already present on the surface of paper fibers as more nanoparticles are added. This could increase the probability of dimerization between nanoparticles, leading to hotspots and increased SERS intensity.[20] When large volumes of Au-MBA conjugates are administered all at once there may be less opportunities for dimerization, reducing the SERS response. Figure 41 summarizes this hypothesis.

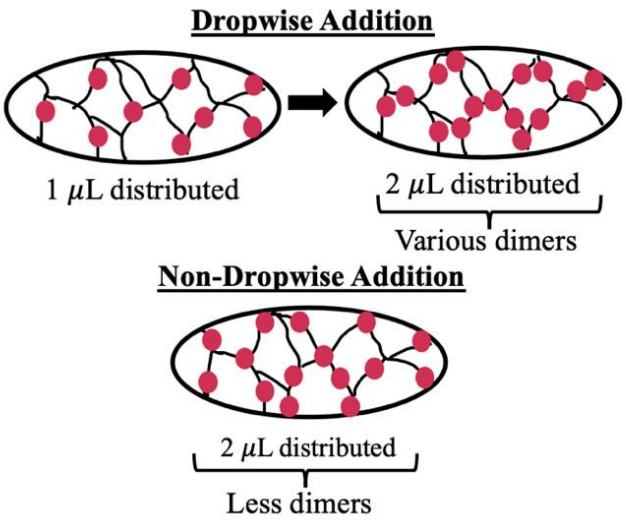

Figure 41. Schematic illustration of the hypothesis in terms of the dropwise administration of NPs leading to the increased presence of dimers and thus hotspots for SERS.

3.7 Determination of the Limit of Detection in Terms of Nanoparticle Coverage

The limit of detection (LOD) is a critical measure of the effectiveness of a biosensor. As such, the limit of detection as a function of gold nanoparticles present on the surface was determined. The conventional method to measure the LOD is dividing three times the standard deviation of the detector noise by the slope of a plot of the signal intensity as a function of concentration. To get a good understanding of noise, dilute solutions of the 60 nm Au-MBA conjugates were tested. A 1 to 4 dilution was initially performed and dropped to volumes of 2.5 μL, 5.0 μL and 7.5 μL, leading to the administration of 3.75×10^7 NPs. A 1 to 3 dilution was then performed and 2.5 μL of the solution was dropped onto the substrate. A single 1 to 2 dilution was performed and dropped, amounting to the addition of 7.92×10^7 gold nanoparticles in total. Figure 42 contains the stacked Raman spectra for each concentration of nanoparticles. Using these spectra, the standard deviation of the noise was found to be 251.2 a.u. Figure 43 contains a plot of the maximum SERS intensity for each concentration at the 1080 cm^{-1} peak.

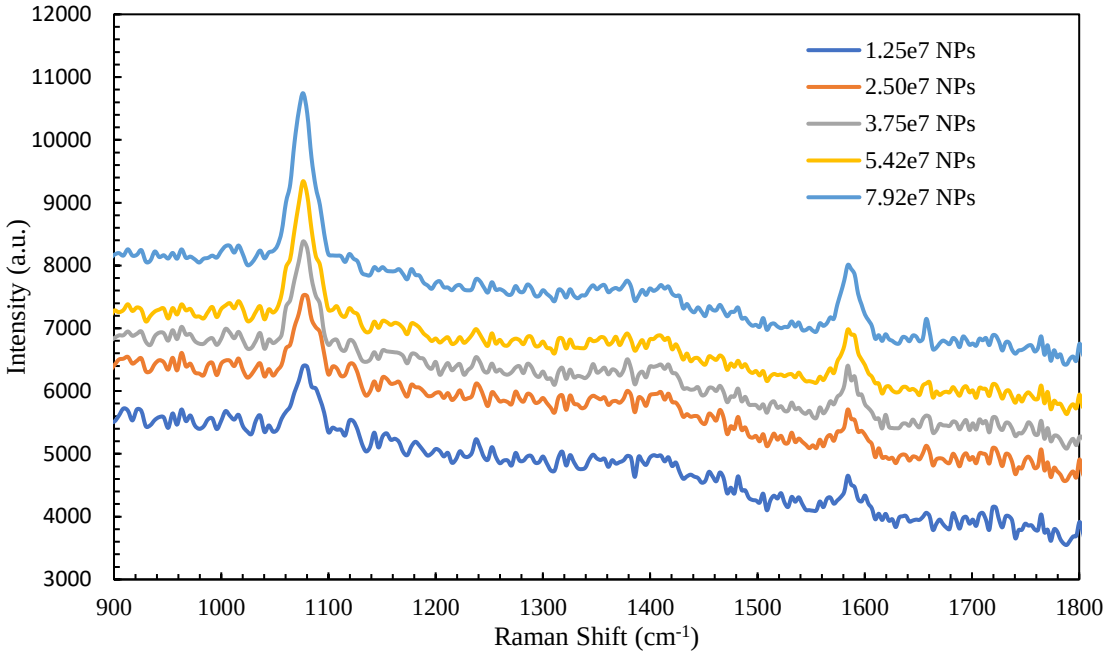

Figure 42. SERS spectra of diluted 60 nm Au-MBA samples generated to determine the signal and noise for LOD analysis.

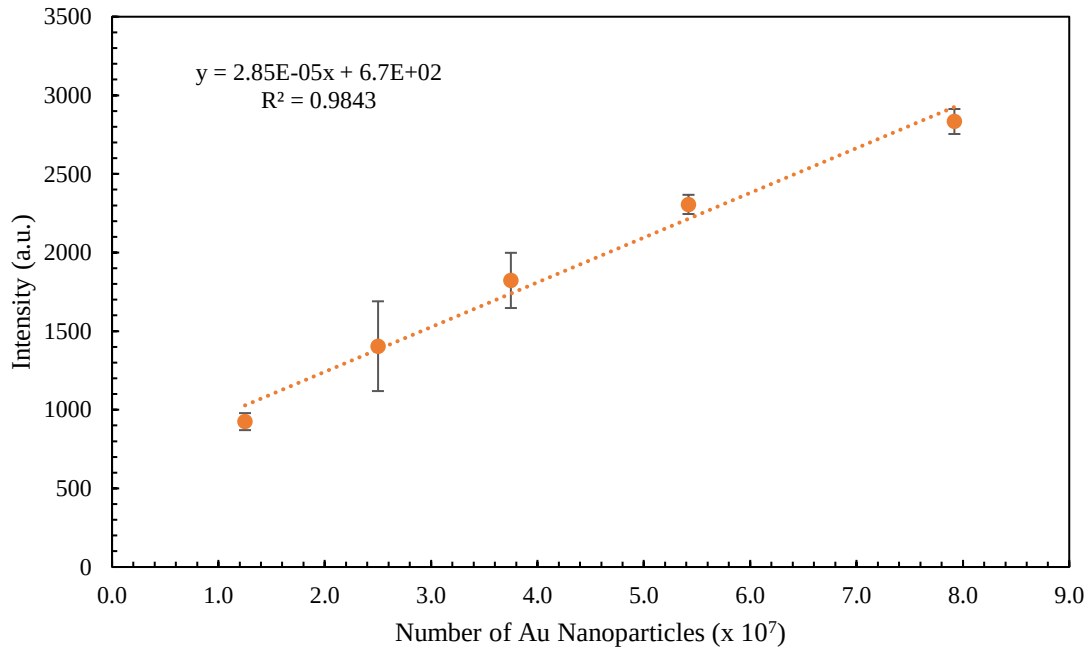

Figure 43. Plot of SERS peak intensity for 60 nm Au-MBA channels without wax at the 1080 cm^{-1} peak after baseline correction with OriginPro.

With the slope of 2.85 x 10^{-5} a.u. NP^{-1} determined, the limit of detection for this platform was found to be 2.64 x 10^{7} gold nanoparticles using equation 4.

$$LOD = \frac{3(251.2 \text{ a.u.})}{2.85 \times 10^{-5} \text{ a.u. } NP^{-1}} \quad (4)$$

To put this number into perspective, calculations were made in relation to the paper channels utilized. The diameter of the circular wells for solution administration was measured to be 0.30 cm, as shown in Figure 44. Using this value, the number of nanoparticles required per square centimeter of the wells at the LOD was found to be 3.74 x 10^{8} NP cm^{-2}, using equation 5. This value suggests that at least 3.74 x 10^{8} NPs must be present in each square centimeter of the wells to obtain a significant signal above the baseline in SERS analysis.

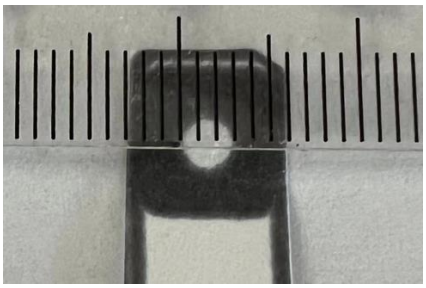

Figure 44. Photo showing the diameter of the SERS circular well used for sample administration.

$$NP/cm^2 = \frac{2.64 \times 10^{7} \text{ NP}}{(\pi)(.15 \text{ cm})^2} \quad (5)$$

Yet, this geometric surface area is not accurate because of the porous nature of the Whatman No.1 paper. The following calculations approximate the surface area of the Whatman paper, accounting for its pore size of 11 μm and its nomial basis of weight of 87 g m^{-2}. The paper additionally has a thickness of 180 μm. Using these values, the density of the paper was calculated to be 4.8 x 10^{-1} g cm^{-3} in equation 6.

$$\text{Density} = 87 \frac{g}{m^2} \left(\frac{1\ m^2}{(10^2)^2\ cm^2} \right) \left(\frac{1}{180\ \mu m} \right) \left(\frac{10^4 \mu m}{1\ cm} \right) \quad (6)$$

The density of densly packed cellulose, however, is 1.5 g cm^{-3}. By taking a density ratio of porous Whatman paper to densly packed cellulose, the volume of the pores was found. The density ratio was found to equal 0.32 in equation 7.

$$\text{Density Ratio} = \frac{4.8 \times 10^{-1} g\ cm^{-3}}{1.5\ g\ cm^{-3}} \quad (7)$$

This means that the void space, made up by pores, amounts to 68% of the paper volume. Assuming the pores are perfect spheres, the void space value was used to determine the number of pores, N, present in 1 cm^3 of the Whatman paper by setting the the void space equal to the number of pores multiplied by the volume of each pore, as shown in equation 8. This equation yieled a value of 9.76 x 10^8 pores, where r is the pore radius of 5.5 μm.

$$N \times \frac{4}{3} \pi (r)^3 = 0.68 \times 1\ cm^3 \quad (8)$$

The total surface area of the three-dimensional paper, accounting for the surface area of the pores, in a single cm^3 was then found to be 3.71 x 10^3 cm^2 by multiplying the number of pores by the surface area of a single pore in equation 9.

$$\text{Surface Area} = N \times 4\pi (r)^2 \quad (9)$$

The surface area per volume of a circular well on the SERS based channels was then determined by accounting for the diameter of 0.30 nm and thickness of 180 μm for a single well, as shown in Figure 44 above. Using these values, the volume of the circular well for solution administration was found to be 1.27 x 10^{-3} cm^3, as shown in equation 10.

$$\text{Volume of substrate well} = \pi (r)^2 x\ \text{thickness} \quad (10)$$

The surface area to volume ratio was then utilized to determine the surface area of the porous Whatman paper in a single circular well, of a volume of 1.27 x 10^{-3} cm^3. The surface area in the ciruclar well was found to be 4.71 cm^2, as shown in equation 11.

$$\frac{3.71 \times 10^{3}\ cm^2}{1\ cm^3} = \frac{\text{Surface Area}}{1.27 \times 10^{-3}\ cm^3} \tag{11}$$

The ratio of nanoparticles per square centimeter of the channel could then be determined in a similar manner as previously for the less accurate geometric surface area of the paper. The amount of nanoparticles required per square centimeter of paper at the LOD was determined to be 5.61 x 10^6 NP cm^{-2} in equation 12.

$$NPs/cm^2 = \frac{2.64 \times 10^{7} NPs}{4.71\ cm^2} \tag{12}$$

To futher put the LOD into perspective, this value was compared to a theoretically densly packed nanoparticle distribution in a 100 packing structure as shown in Figure 45. Under this packing style, a single unit cell contains 1 nanoparticle, as demostrated.

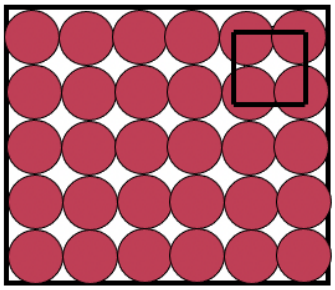

Figure 45. Schematic representation of a theoretical monolayer of gold nanoparticles packed in (100) on the surface, with a single unit cell denoted by the square.

The amount of 60 nm gold nanoparticles per square centimeter in a theoretical monolayer was then found to be 2.78 x 10^{10} NPs cm^{-2} using equation 13, where the area of a unit cell is equal to the squared diameter of the nanoparticles.

$$\text{NPs/unit cell} = \frac{1 \text{ nanoparticle}}{((60 \text{ nm})(\frac{10^{-7} \text{ cm}}{1 \text{ nm}}))^2} \quad (13)$$

$$= 2.78 \times 10^{10} \text{ NPs cm}^{-2}$$

Therefore, 2.78×10^{10} gold nanoparticles are required per square centimeter for a single monolayer of theorically densly packed nanoparticles. For the less accurate geometric surface area calculated in equation 5, the ratio of nanoparticles per square centimeter at the LOD to the nanoparticles per square centimeter for a single monolayer was found to be 0.014 in equation 14. This suggests that the nanoparticles required for the LOD account for **1.4%** of a theoretical gold nanoparticle monolayer. As shown in equation 15, the ratio using the more accurate surface area was found to equal 0.00020. This indicates that the LOD of gold nanoparticles represents only **0.020%** of the nanoparticles required for one monolayer of theoretical dense packing.

$$\frac{3.74 \times 10^{8} \text{ NP cm}^{-2}}{2.78 \times 10^{10} \text{ NPs cm}^{-2}} \quad (14)$$

$$\frac{5.61 \times 10^{6} \text{ NP cm}^{-2}}{2.78 \times 10^{10} \text{ NPs cm}^{-2}} \quad (15)$$

4. SUMMARY AND FUTURE WORK

This study aimed to optimize the use of paper-based substrates for SERS analysis to determine the ideal substrate preparation procedures for a biosensor. It was found that channels without wax backing showed better linearity and sensitivity as compared to channels with wax backing. This result was consistent among drying modes (i.e. horizontal vs. vertical) and nanoparticle sizes ranging from 30 nm to 60 nm. While it is likely that this result can be conceptualized as a consequence of a higher degree of uniformity in nanoparticle distribution on paper as a result of two-directional

evaportation for no wax backing substrates, future analyses should utilize scanning electron microscopy to visualize the placement of nanoparticles on paper fibers.

This analysis also revealed a LOD amounting to 0.020% of a single monolayer of gold nanoparticles. This result points to the large extent of surface enhancement at low concentrations of gold nanoparticles. It can be attributed with the strong surface plasmon resonance band of gold nanoparticles.[48] Future analyses should investigate how the LOD of wax-backed channels compares to non-waxed backed channels, as well as if nanoparticle size contributes to the measured LOD.

With this understanding of optimal drying procedures, and the LOD, efforts have been made to expand this platform for use as a biosensor to detect SARS-CoV-2. To achieve this goal, detection and capture N-protein antibodies are conjugated to MBA via click chemistry with the crosslinkers 1-Ethyl-3-(3-dimethylaminopropyl) carbodiimide (EDC) and Sulfo-NHS (N-hydroxysulfosuccinimide) (S-NHS).[49] For bioconjugation to occur, MBA must first attach to the nanoparticle surface by means of the thiol (-SH) functional group. The crosslinker EDC can then interact with the carboxylic acid of MBA through the carbodiimide functional group, forming an unstable intermediate known as O-acylisourea. The S-NHS crosslinker can then replace the EDC attached to the MBA carboxylic acid, forming an ester. The N-protein antibody is then able to form an amide bond at the MBA carboxylic acid. [49] An important note is that not all MBA molecules are attached to antibodies due to steric hinderance. Some O-acylisourea can also directly form an amide bond between MBA and a primary amine, and some is hydrolyzed in solution. [49] Figures 45 and 46 display an overview of this process.

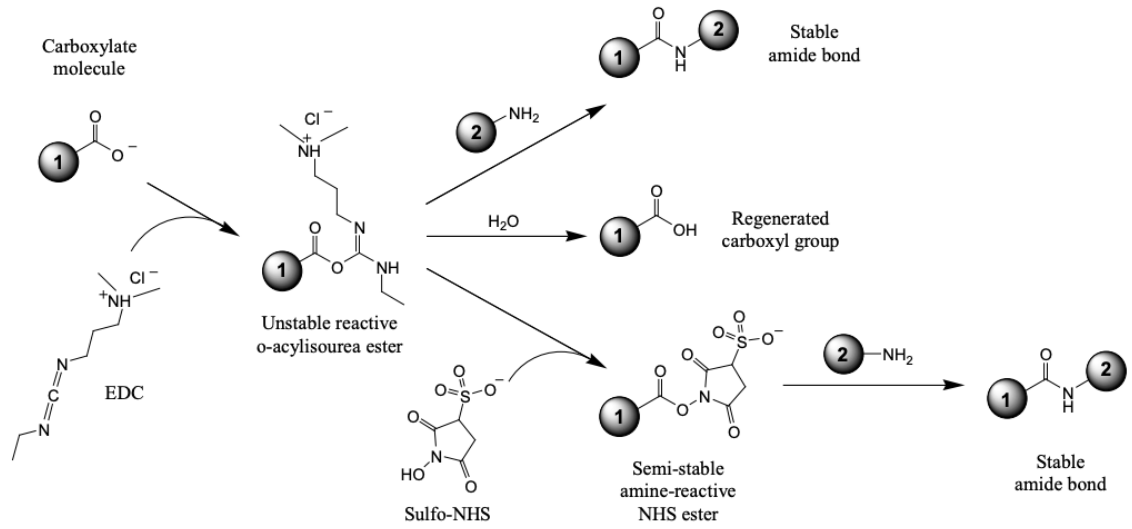

Figure 46. Illustrations of the click chemistry reaction between MBA, S-NHS, EDC, and the N-protein antibody. The reaction begins with the attachment of the crosslinker EDC to the carboxylic acid of MBA, labeled 1, forming the unstable intermediate O-acylisourea. This intermediate can then be hydrolyzed, directly interact with the primary amine antibody, or be replaced by S-NHS to form an ester. An amide bond can then be formed by replacement of S-NHS with the primary amine antibody at MBA's carboxylic acid (Reprinted from Thermo Fisher).[50]

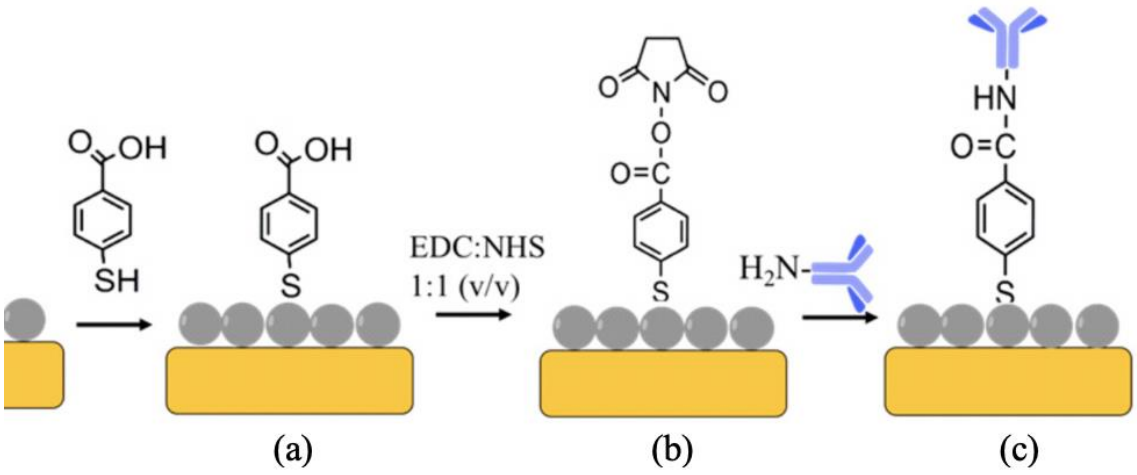

Figure 47. Procedure to create a bio-conjugated nanoprobe via MBA, S-NHS, and EDC click chemistry, including: (a) the conjugation of MBA, (b) the binding of EDC and NHS to MBA, and (c) the formation of an amide bond between MBA and the SARS-CoV-2 antibody (Reprinted and edited from Téllez-Plancarte et. al., 2018). [51]

Once the nanocomposite biosensor is developed through bioconjugation, it can be used to detect the presence or absence of SARS-CoV-2 N-protein antigens. If present, the

antigens will be captured by the antibodies in a formation called a sandwich structure between the detection and capture antibodies.[52] While both detection and capture antibodies bind the N-protein, the location of their binding epitope varies, providing an extra degree of selectivity. [52] By bringing nanoparticles in close proximity, the sandwich structure, shown in Figure 48, significantly increases the SERS intensity via the formation of hotspots.[53] Due to the signal increase accompanied with the binding of N-protein antigens, a change in the SERS intensity can be correlated with the presence of an N-protein antigen in a concentration dependent manner.

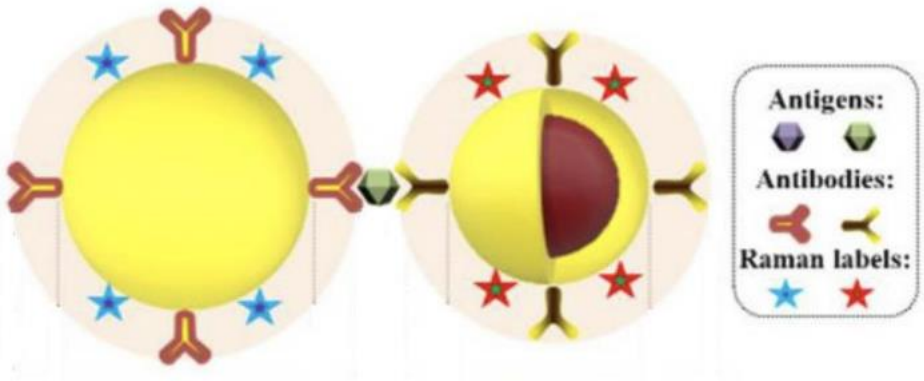

Figure 48. Schematic representation of the sandwich complex formed between the nanoparticle-conjugated detection and capture antibodies when bound to an N-protein antigen, leading to the formation of a hotspot between the nanoparticles (Reprinted and edited from Cheng et al., 2021). [53]

Some preliminary work in the Zhong group has tested the use of this nanocomposite biosensor for the detection of N-protein antigens. It was found that when 80 ng mL^{-1} of N-protein was added to the biosensor, a 4-fold increase in the SERS intensity resulted, demonstrating the potential for this platform to serve as a biosensor for SARS-CoV-2. In the future, additional concentrations of N-protein antigens, as well as live virus samples will be tested to better conceptualize the sensitivity and selectivity of

this platform in the detection of SARS-CoV-2. Additionally, due to the use of paper substrates and the versatility of click chemistry, this methodology can be expanded to detect additional diseases through the bioconjugation of known antibodies for human disorders. The use of paper-based substrates also presents the possibility for multiplexing by performing separate bioconjugation reactions in paper channels.

References

(1) Naresh, Varnakavi.; Lee, N. A Review on Biosensors and Recent Development of Nanostructured Materials-Enabled Biosensors. *Sensors* **2021**, *21* (4), 1109. https://doi.org/10.3390/s21041109.

(2) Bhalla, N.; Jolly, P.; Formisano, N.; Estrela, P. Introduction to Biosensors. *Essays in Biochemistry* **2016**, *60* (1), 1–8. https://doi.org/10.1042/EBC20150001.

(3) Dincer, C.; Bruch, R.; Costa-Rama, E.; Fernández-Abedul, M. T.; Merkoçi, A.; Manz, A.; Urban, G. A.; Güder, F. Disposable Sensors in Diagnostics, Food, and Environmental Monitoring. *Advanced Materials* **2019**, 1806739. https://doi.org/10.1002/adma.201806739.

(4) Pilot; Signorini; Durante; Orian; Bhamidipati; Fabris. A Review on Surface-Enhanced Raman Scattering. *Biosensors (Basel)* **2019**, *9* (2), 57. https://doi.org/10.3390/bios9020057.

(5) Li, J.; Skeete, Z.; Shan, S.; Yan, S.; Kurzatkowska, K.; Zhao, W.; Ngo, Q. M.; Holubovska, P.; Luo, J.; Hepel, M.; Zhong, C.-J. Surface Enhanced Raman Scattering Detection of Cancer Biomarkers with Bifunctional Nanocomposite Probes. *Analytical Chemistry* **2015**, *87* (21), 10698–10702. https://doi.org/10.1021/acs.analchem.5b03456.

(6) Link, S.; El-Sayed, M. A. Shape and Size Dependence of Radiative, Non-Radiative and Photothermal Properties of Gold Nanocrystals. *International Reviews in Physical Chemistry* **2000**, *19* (3), 409–453. https://doi.org/10.1080/01442350050034180.

(7) McCreery, R. L. *Raman Spectroscopy for Chemical Analysis*; John Wiley & Sons, Inc.: Hoboken, NJ, USA, 2000; Vol. 157. https://doi.org/10.1002/0471721646.

(8) Kim, Y.; Jeong, S.; Jun, B.-H.; Lee, Y.-S.; Lee, Y.-S.; Jeong, D. H.; Lee, D. S. Endoscopic Imaging Using Surface-Enhanced Raman Scattering. *European Journal of Nanomedicine* **2017**, *9* (3–4). https://doi.org/10.1515/ejnm-2017-0005.

(9) Fleischmann, M.; Hendra, P. J.; McQuillan, A. J. Raman Spectra of Pyridine Adsorbed at a Silver Electrode. *Chemical Physics Letters* **1974**, *26* (2), 163–166. https://doi.org/10.1016/0009-2614(74)85388-1.

(10) Jeanmaire, D. L.; van Duyne, R. P. Surface Raman Spectroelectrochemistry. *Journal of Electroanalytical Chemistry and Interfacial Electrochemistry* **1977**, *84* (1), 1–20. https://doi.org/10.1016/S0022-0728(77)80224-6.

(11) Albrecht, M. G.; Creighton, J. A. Anomalously Intense Raman Spectra of Pyridine at a Silver Electrode. *J Am Chem Soc* **1977**, *99* (15), 5215–5217. https://doi.org/10.1021/ja00457a071.

(12) le Ru, E.; Etchegoin, P. *Principles of Surface-Enhanced Raman Spectroscopy*; Elsevier, 2009. https://doi.org/10.1016/B978-0-444-52779-0.X0001-3.

(13) Amendola, V.; Pilot, R.; Frasconi, M.; Maragò, O. M.; Iatì, M. A. Surface Plasmon Resonance in Gold Nanoparticles: A Review. *Journal of Physics: Condensed Matter* **2017**, *29* (20), 203002. https://doi.org/10.1088/1361-648X/aa60f3.

(14) Willets, K. A.; van Duyne, R. P. Localized Surface Plasmon Resonance Spectroscopy and Sensing. *Annual Review of Physical Chemistry* **2007**, *58* (1), 267–297. https://doi.org/10.1146/annurev.physchem.58.032806.104607.

(15) Mie, G. Beiträge Zur Optik Trüber Medien, Speziell Kolloidaler Metallösungen. *Ann Phys* **1908**, *330* (3), 377–445. https://doi.org/10.1002/andp.19083300302.
(16) Tauran, Y.; Brioude, A.; Coleman, A. W.; Rhimi, M.; Kim, B. Molecular Recognition by Gold, Silver and Copper Nanoparticles. *World Journal of Biological Chemistry* **2013**, *4* (3), 35. https://doi.org/10.4331/wjbc.v4.i3.35.
(17) Goy, P.; Raimond, J. M.; Gross, M.; Haroche, S. Observation of Cavity-Enhanced Single-Atom Spontaneous Emission. *Physical Review Letters* **1983**, *50* (24), 1903–1906. https://doi.org/10.1103/PhysRevLett.50.1903.
(18) le Ru, E. C.; Meyer, M.; Blackie, E.; Etchegoin, P. G. Advanced Aspects of Electromagnetic SERS Enhancement Factors at a Hot Spot. *Journal of Raman Spectroscopy* **2008**, *39* (9), 1127–1134. https://doi.org/10.1002/jrs.1945.
(19) Etchegoin, P. G.; le Ru, E. C. A Perspective on Single Molecule SERS: Current Status and Future Challenges. *Physical Chemistry Chemical Physics* **2008**, *10* (40), 6079. https://doi.org/10.1039/b809196j.
(20) le Ru, E. C.; Galloway, C.; Etchegoin, P. G. On the Connection between Optical Absorption/Extinction and SERS Enhancements. *Physical Chemistry Chemical Physics* **2006**, *8* (26), 3083. https://doi.org/10.1039/b605292d.
(21) Radziuk, D.; Moehwald, H. Prospects for Plasmonic Hot Spots in Single Molecule SERS towards the Chemical Imaging of Live Cells. *Physical Chemistry Chemical Physics* **2015**, *17* (33), 21072–21093. https://doi.org/10.1039/C4CP04946B.
(22) Otto, A. The 'Chemical' (Electronic) Contribution to Surface-Enhanced Raman Scattering. *Journal of Raman Spectroscopy* **2005**, *36* (6–7), 497–509. https://doi.org/10.1002/jrs.1355.
(23) Lombardi, J. R.; Birke, R. L. A Unified View of Surface-Enhanced Raman Scattering. *Accounts of Chemical Research* **2009**, *42* (6), 734–742. https://doi.org/10.1021/ar800249y.
(24) Aroca, R. *Surface-Enhanced Vibrational Spectroscopy*; John Wiley & Sons, Ltd: Chichester, UK, 2006. https://doi.org/10.1002/9780470035641.
(25) Sarkar, A.; Paul, B. The Global Menace of Arsenic and Its Conventional Remediation - A Critical Review. *Chemosphere* **2016**, *158*, 37–49. https://doi.org/10.1016/j.chemosphere.2016.05.043.
(26) Jensen, L.; Aikens, C. M.; Schatz, G. C. Electronic Structure Methods for Studying Surface-Enhanced Raman Scattering. *Chemical Society Reviews* **2008**, *37* (5), 1061. https://doi.org/10.1039/b706023h.
(27) Long, D. A. *The Raman Effect : A Unified Treatment of the Theory of Raman Scattering by Molecules*; Wiley, 2002.
(28) Chu, H.; Song, S.; Li, C.; Gibson, D. Surface Enhanced Raman Scattering Substrates Made by Oblique Angle Deposition: Methods and Applications. *Coatings* **2017**, *7* (2), 26. https://doi.org/10.3390/coatings7020026.
(29) Xu, K.; Zhou, R.; Takei, K.; Hong, M. Toward Flexible Surface-Enhanced Raman Scattering (SERS) Sensors for Point-of-Care Diagnostics. *Advanced Science* **2019**, *6* (16), 1900925. https://doi.org/10.1002/advs.201900925.
(30) Vo-Dinh, Tuan.; Hiromoto, M. Y. K.; Begun, G. M.; Moody, R. L. Surface-Enhanced Raman Spectrometry for Trace Organic Analysis. *Analytical Chemistry* **1984**, *56* (9), 1667–1670. https://doi.org/10.1021/ac00273a029.

(31) Lee, C. H.; Tian, L.; Singamaneni, S. Paper-Based SERS Swab for Rapid Trace Detection on Real-World Surfaces. *ACS Applied Materials & Interfaces* **2010**, *2* (12), 3429–3435. https://doi.org/10.1021/am1009875.
(32) Azizi Samir, M. A. S.; Alloin, F.; Dufresne, A. Review of Recent Research into Cellulosic Whiskers, Their Properties and Their Application in Nanocomposite Field. *Biomacromolecules* **2005**, *6* (2), 612–626. https://doi.org/10.1021/bm0493685.
(33) Berthod, A.; Laserna, J. J.; Winefordner, J. D. Analysis by Surface Enhanced Raman Spectroscopy on Silver Hydrosols and Silver Coated Filter Papers. *Journal of Pharmaceutical and Biomedical Analysis* **1988**, *6* (6–8), 599–608. https://doi.org/10.1016/0731-7085(88)80073-6.
(34) Yu, W. W.; White, I. M. Inkjet Printed Surface Enhanced Raman Spectroscopy Array on Cellulose Paper. *Analytical Chemistry* **2010**, *82* (23), 9626–9630. https://doi.org/10.1021/ac102475k.
(35) Kim, W.; Kim, Y.-H.; Park, H.-K.; Choi, S. Facile Fabrication of a Silver Nanoparticle Immersed, Surface-Enhanced Raman Scattering Imposed Paper Platform through Successive Ionic Layer Absorption and Reaction for On-Site Bioassays. *ACS Applied Materials & Interfaces* **2015**, *7* (50), 27910–27917. https://doi.org/10.1021/acsami.5b09982.
(36) Martinez, A. W.; Phillips, S. T.; Butte, M. J.; Whitesides, G. M. Patterned Paper as a Platform for Inexpensive, Low-Volume, Portable Bioassays. *Angewandte Chemie International Edition* **2007**, *46* (8), 1318–1320. https://doi.org/10.1002/anie.200603817.
(37) Oliveira, M. J.; Quaresma, P.; Peixoto de Almeida, M.; Araújo, A.; Pereira, E.; Fortunato, E.; Martins, R.; Franco, R.; Águas, H. Office Paper Decorated with Silver Nanostars - an Alternative Cost Effective Platform for Trace Analyte Detection by SERS. *Scientific Reports* **2017**, *7* (1), 2480. https://doi.org/10.1038/s41598-017-02484-8.
(38) Restaino, S. M.; White, I. M. A Critical Review of Flexible and Porous SERS Sensors for Analytical Chemistry at the Point-of-Sample. *Analytica Chimica Acta* **2019**, *1060*, 17–29. https://doi.org/10.1016/j.aca.2018.11.057.
(39) Polte, J. Fundamental Growth Principles of Colloidal Metal Nanoparticles – a New Perspective. *CrystEngComm* **2015**, *17* (36), 6809–6830. https://doi.org/10.1039/C5CE01014D.
(40) Ho, C.-H.; Lee, S. SERS and DFT Investigation of the Adsorption Behavior of 4-Mercaptobenzoic Acid on Silver Colloids. *Colloids and Surfaces A: Physicochemical and Engineering Aspects* **2015**, *474*, 29–35. https://doi.org/10.1016/j.colsurfa.2015.03.004.
(41) Zhong, C.; Njoki, P.; Luo, J. Controlled Synthesis of Highly Monodispersed Gold Nanoparticles. 7,524,354 B2, 2009.
(42) Link, S.; El-Sayed, M. A. Size and Temperature Dependence of the Plasmon Absorption of Colloidal Gold Nanoparticles. *The Journal of Physical Chemistry B* **1999**, *103* (21), 4212–4217. https://doi.org/10.1021/jp984796o.
(43) Njoki, P. N.; Lim, I.-I. S.; Mott, D.; Park, H.-Y.; Khan, B.; Mishra, S.; Sujakumar, R.; Luo, J.; Zhong, C.-J. Size Correlation of Optical and Spectroscopic Properties

for Gold Nanoparticles. *The Journal of Physical Chemistry C* **2007**, *111* (40), 14664–14669. https://doi.org/10.1021/jp074902z.
(44) Jain, P. K.; Huang, X.; El-Sayed, I. H.; El-Sayed, M. A. Review of Some Interesting Surface Plasmon Resonance-Enhanced Properties of Noble Metal Nanoparticles and Their Applications to Biosystems. *Plasmonics* **2007**, *2* (3), 107–118. https://doi.org/10.1007/s11468-007-9031-1.
(45) Guo, D.; Xie, G.; Luo, J. Mechanical Properties of Nanoparticles: Basics and Applications. *Journal of Physics D: Applied Physics* **2014**, *47* (1), 013001. https://doi.org/10.1088/0022-3727/47/1/013001.
(46) Marturi, N. Vision and Visual Servoing for Nanomanipulation and Nanocharacterization in Scanning Electron Microscope., 2013.
(47) Njoki, P. N.; Luo, J.; Kamundi, M. M.; Lim, S.; Zhong, C.-J. Aggregative Growth in the Size-Controlled Growth of Monodispersed Gold Nanoparticles. *Langmuir* **2010**, *26* (16), 13622–13629. https://doi.org/10.1021/la1019058.
(48) Hoque, M. M.; Mayer, K. M.; Ponce, A.; Alvarez, M. M.; Whetten, R. L. Toward Smaller Aqueous-Phase Plasmonic Gold Nanoparticles: High-Stability Thiolate-Protected ∼4.5 Nm Cores. *Langmuir* **2019**, *35* (32), 10610–10617. https://doi.org/10.1021/acs.langmuir.9b01908.
(49) Greg Hermanson. *Bioconjugate Techniques*, 3rd Edition.; 2013.
(50) ThermoScientific. *Instructions NHS and Sulfo-NHS*; Rockford, IL, 2011.
(51) Téllez-Plancarte, A.; Haro-Poniatowski, E.; Picquart, M.; Morales-Méndez, J.; Lara-Cruz, C.; Jiménez-Salazar, J.; Damián-Matsumura, P.; Escobar-Alarcón, L.; Batina, N. Development of a Nanostructured Platform for Identifying HER2-Heterogeneity of Breast Cancer Cells by Surface-Enhanced Raman Scattering. *Nanomaterials* **2018**, *8* (7), 549. https://doi.org/10.3390/nano8070549.
(52) Cox, K. L.; Devanarayan, V.; Kriauciunas, A.; Manetta, J.; Montrose, C.; Sittampalam, S. *Immunoassay Methods*; 2004.
(53) Cheng, H.-W.; Xue, S.-Y.; Li, J.; Gordon, J. S.; Wang, S.; Filippone, N. R.; Ngo, Q. M.; Zhong, C.-J. Assessing Plasmonic Nanoprobes in Electromagnetic Field Enhancement for SERS Detection of Biomarkers. *Sensors* **2021**, *21* (24), 8345. https://doi.org/10.3390/s21248345.